High-Resolution Numerical Simulation of the Extreme Rainfall Associated with Typhoon Morakot. Part I: Comparing the Impact of Microphysics and PBL Parameterizations with Observations

Wei-Kuo Tao [1,*], Jainn Jong Shi [1,2], Pay-Liam Lin [3], Jhihying Chen [3], Stephen Lang [1,4], Mei-Yu Chang [5], Ming-Jen Yang [3], Chun-Chien Wu [6], Christa Peters-Lidard [7], Chung-Hsiung Sui [6], and Ben Jong-Dao Jou [6]

[1] *Laboratory for Atmospheres, NASA Goddard Space Flight Center, Greenbelt, Maryland, USA*
[2] *Goddard Earth Sciences and Technology Center, University of Maryland at Baltimore County, Maryland, USA*
[3] *Department of Atmospheric Science, National Central University, Jhongli, Taiwan, ROC*
[4] *Science Systems and Applications, Inc., Lanham, Maryland, USA*
[5] *Central Weather Bureau, Taipei, Taiwan, ROC*
[6] *Department of Atmospheric Sciences, National Taiwan University, Taipei, Taiwan, ROC*
[7] *Hydrological Sciences Branch, NASA Goddard Space Flight Center, Greenbelt, Maryland, USA*

ABSTRACT

Typhoon Morakot hit Taiwan the night of 7 August 2009 as a Category 1 storm and caused up to 3000 mm of rain, leading to the worst flooding there in 50 years as well as devastating mudslides. The Weather Research and Forecasting model (WRF) is used at high resolution to simulate this extreme weather event. The model results indicate that WRF is able to capture the amount and location of the observed surface rainfall and that the typhoon-induced circulation, orographic lifting and a moisture-abundant southwest flow are the main mechanisms that together produced the tremendous rainfall in this case. Furthermore, the model results suggest that the agreement with the observed rainfall is due to the simulated storm track and intensity being in relatively good agreement with the observed. Additional simulations were made to examine the sensitivity of this case to model physics (microphysics and planetary boundary layer or PBL). Both warm rain only as well as improved microphysics yield similar significant rain amounts at the same locations as the control case. The improved microphysics lead to a better storm intensity early on but later exceed the observed intensities by about 10 hPa. The stronger storm arises from less evaporative cooling from cloud and rain and consequently weaker simulated downdrafts. Warm rain results closely match the control (i.e., the track, intensity, and maximum rainfall locations/amounts), implying ice processes (i.e., additional heat release due to ice processes) have only a secondary effect on surface rainfall. Results are less sensitive to using different PBL schemes than different microphysics.

1. INTRODUCTION

Continuing advances in computing power are allowing atmospheric prediction models to be run at progressively finer scales of resolution, using increasingly more sophisticated physical parameterizations and numerical methods. The representation of cloud microphysical processes is a key component of these models, and during the past decade both research and operational numerical weather prediction (NWP) models have started using more complex microphysical schemes originally developed from high-resolution cloud-resolving models (CRMs). CRMs, which are run at horizontal resolutions on the order of 1 - 2 km or less, explicitly simulate complex dynamical and microphysical processes associated with deep, precipitating atmospheric convection. Because operational NWP models are run at coarser resolutions, the effects of atmospheric convection

* Corresponding author
  E-mail: wei-kuo.tao-1@nasa.gov

must be parameterized, leading to large sources of error that most dramatically affect quantitative precipitation forecasts (QPF). A report to the United States Weather Research Program (USWRP) Science Steering Committee specifically calls for the replacement of implicit cumulus parameterization schemes with explicit bulk schemes in NWP as part of a community effort to improve quantitative precipitation forecasts (Fritsch and Carbone 2002). It is not clear, however, whether such a strategy alone will resolve the difficult and outstanding challenges that face mesoscale NWP. Some operational weather centers are, in fact, attempting to unify physics development, including the use of cloud parameterization schemes over a wide range of temporal and spatial scales of motion.

There is no doubt that cloud microphysics play an important role in non-hydrostatic high-resolution simulations as evidenced by the extensive amount of research devoted to the development and improvement of cloud microphysical schemes and their application to the study of precipitation processes, hurricanes and other severe weather events over the past two and a half decades (see Table 1 shown in Tao et al. 2011). Many different approaches have been used to examine the impact of microphysics on precipitation processes associated with convective systems and hurricanes and typhoons (see a review by Tao et al. 2011). Only a few modeling studies have investigated microphysics in tropical cyclones and hurricanes using high-resolution (i.e., about 5 km or less) numerical models. In general, all of the studies show that microphysics schemes do not have a major impact on track forecasts but do have more of an effect on the simulated intensity. Also, nearly all of the previous studies found that simulated hurricanes had the strongest deepening or intensification when using only warm rain physics. This is because all of the simulated precipitating hydrometeors are large raindrops that quickly fall out near the eye-wall region where a large amount of latent heat is released in the middle troposphere, which would hydrostatically produce the lowest pressure near the surface. In contrast, latent heat release occurs over a larger area including the eye-wall and outer rain-band regions if ice-phase microphysics is included. In addition, these studies suggested that intensities become unrealistically strong when evaporative cooling from cloud droplets and melting from ice particles are removed,

because it results in much weaker downdrafts in the simulated storms.

Anthes and Chang (1978) indicated that the planetary boundary layer (PBL) processes in a numerical model could have a substantial impact on simulated hurricane intensity. Based on the numerical simulations of Hurricane Bob (1991), Braun and Tao (2000) showed that different PBL schemes in the Fifth-Generation NCAR/Penn State Mesoscale Model (MM5) could lead to differences of 16 hPa in the central pressure and 15 m s^{-1} in the maximum surface wind during a 72-h simulation period. In particular, Braun and Tao found that the larger exchange coefficients of enthalpy and momentum in the PBL schemes could lead to stronger storm intensities. Li and Pu (2008) investigated the sensitivity of simulations during the early rapid intensification of Hurricane Emily (2005) to cloud microphysics and PBL schemes. They showed that different PBL schemes produced differences of up to 19 hPa in the simulated central pressure during the 30-h forecast period. Nolan et al. (2009a, b) examined the simulated PBL structures of Hurricane Isabel (2003) in the Weather Research and Forecasting model (WRF, a state-of-the-art regional numerical model, Skamarock et al. 2008) using *in situ* data obtained during the Coupled Boundary Layer and Air-Sea Transfer Experiment (CBLAST) by comparing the simulations using the Yonsei University (YSU) parameterization and the Mellor-Yamada-Janjić (MYJ) parameterization. They found that both PBL schemes simulated the boundary-layer structures reasonably well. With or without the ocean roughness-length correction, the MYJ scheme consistently produced larger frictional tendencies in the PBL than the YSU scheme, resulting in a lower central pressure, a stronger low-level inflow and a stronger tangential wind maximum at the top of the PBL. The precipitation associated with tropical cyclones is further complicated by the presence of terrain, such as Taiwan (Wu and Kuo 1999), in which the treatment of the terrain, as well as its resolution, is crucial for model simulations and forecasts of tropical cyclone tracks and rainfall (Wu et al. 2001, 2002; Jian and Wu 2008; Huang et al. 2011).

The main objective of this paper is to use a regional cloud-scale model with very high resolution (i.e., WRF) to simulate the extreme heavy surface rainfall associated with Typhoon Morakot (2009). Specifically, the study will (1)

Table 1. Microphysics and PBL schemes used in the sensitivity tests for the Morakot case.

Case	Microphysics	PBL
Control	3ICE with graupel (Lang et al. 2007)	Mellor-Yamada-Janjić (Mellor and Yamada 1992)
Warm Rain	No Ice (Soong and Ougra 1973)	MYJ
Improved	3ICE with graupel (Lang et al. 2011)	MYJ
YSU	3ICE with graupel (Lang et al. 2007)	Yonsei University PBL scheme (Hong et al. 2006)

examine WRF's ability to simulate the extreme heavy precipitation, (2) compare the simulated heavy precipitation with that which was observed, (3) investigate the impact of the microphysical schemes on the heavy rainfall, and (4) investigate the impact of the PBL processes on this heavy precipitation event. This paper is the first of three parts on the modeling of Typhoon Morakot. Orographic effects and sensitivity to model resolution will be the focus of Part II with momentum transport and the water budget the focus of Part III.

2. A BRIEF DESCRIPTION OF TYPHOON MORA-KOT (2009)

Morakot began as a tropical depression on the morning of 2 August 2009 in the central Philippine Sea about midway between the Northern Mariana Islands and Taiwan. The system strengthened into a tropical storm later on the 3rd and became a typhoon on the morning of the 5th as is tracked due westward toward Taiwan. Morakot maintained Category 1 intensity on the 6th and 7th with sustained winds estimated at 80 knots (~92 mph) by the Joint Typhoon Warning Center. Typhoon Morakot struck Taiwan on the night of Friday 7 August 2009 (local time) as a Category 1 storm with sustained winds of 80 knots (~92 mph). Although the center made landfall in Hualien County along the central east coast of Taiwan and passed over the central northern part of the island, it was southern Taiwan that received the worst effects of the storm. According to TRMM-based satellite estimates, nearly the entire southern half of the island received in excess of 600 mm (~24 inches) of rain. Within that were two areas estimated to be in excess of 1000 mm (~40 inches) along the western slopes of the

Central Mountain Range (CMR). The enormous amount of rain resulted in massive flooding, the worst in 50 years, and devastating mudslides. Nearly 700 people lost their life, most in the village of Shiao-Lin, which was destroyed by a large mudslide.

An analysis by Hong et al. (2010) indicated that Typhoon Morakot originated in a large-scale monsoon gyre in the northwestern Pacific where moist southwesterly monsoon flow meets southeasterlies at the western end of the subtropical Pacific high. Morakot was embedded in a large-scale cyclonic circulation associated with the cyclonic phase of a northward moving 40-to-50-day oscillation and a northwestward-moving 10-to-30-day disturbance. The latter is consistent with the climatological features of quasi-biweekly oscillations over the northwestern Pacific (e.g., Chen and Sui 2010) and was the main supply of moisture for the extreme event. It suggests that the multi-scale interaction between the typhoon, the large-scale circulation and the steep topography of southern Taiwan were the key factors leading to this extreme event.

3. MODEL SET UP

WRF V3.1.1 with improved microphysics was used to simulate this case. Figure 1 shows the WRF grid configuration, which includes an outer domain and two inner-nested domains, having 18-, 6- and 2-km horizontal resolution and $391 \times 322 \times 61$, $475 \times 427 \times 61$, $538 \times 439 \times 61$ grid points, respectively. The respective time steps were 18, 6 and 2
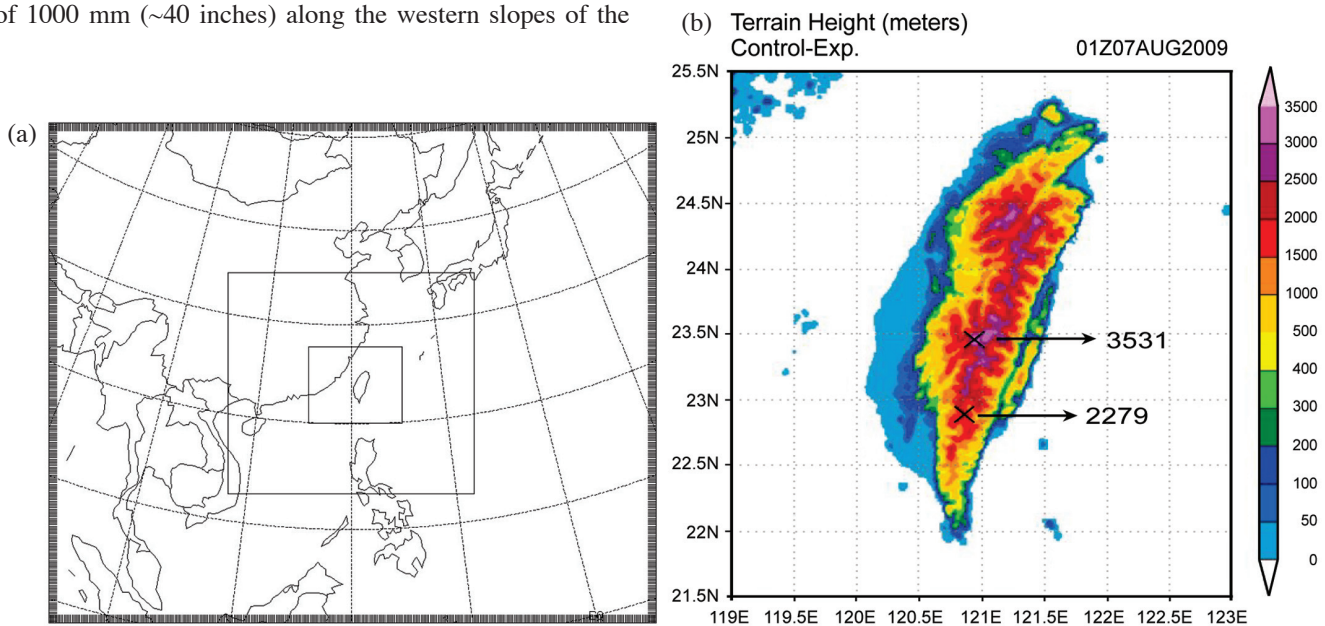

Fig. 1. (a) WRF nested domain configuration used for the Typhoon Morakot case. The horizontal domain resolutions are 18, 6 and 2 km for the outer, middle, and inner domains respectively. (b) The model terrain height over the inner domain, which had a 2-km horizontal resolution that was smoothed from a 30-second (~0.9 km) terrain database.

seconds. The model terrain had a 2-km horizontal resolution that was smoothed from a 30-second (~0.9 km) terrain database. The highest terrain within the 2-km domain was 3531 m (Fig. 1b). The Grell and Dévényi (2002) cumulus parameterization scheme was used for the outer grid (18 km) only. For the inner two domains (6- and 2-km), the scheme was turned off. The surface heat and moisture fluxes (for both land and ocean) were computed using a similarity theory (Monin and Obukhov 1954). The land surface model, based on Chen and Dudhia (2001), is a 4-layer soil temperature and moisture model with canopy moisture and snow cover prediction. The Goddard broadband two-stream (up and downward fluxes) approach was used for the shortwave and longwave radiative flux calculations (Chou and Suarez 1999). The model was initialized from NOAA/NCEP/GFS global analyses (1.0° by 1.0°). Time-varying lateral boundary conditions were provided at 6-h intervals. The heavy rainfall over southern Taiwan occurred from 8 to 9 August 2009, so 72-h integrations were performed starting at 0000 UTC 7 August and ending at 0000 UTC 10 August 2009.

Table 1 shows the numerical simulations performed in this study. These include sensitivity studies on the impact of the microphysics schemes [original 3ICE (three-class ice) with cloud-ice, snow and graupel versus warm rain only versus improved 3ICE wherein 40 dBZ echoes are reduced aloft] and the PBL parameterizations (MYJ versus YSU) on the precipitation processes and surface rainfall associated with Typhoon Morakot. Details on the improved Goddard microphysics and the two PBL schemes are described in Appendix A and B, respectively.

4. COMPARISON WITH OBSERVATIONS

The observed and simulated minimum sea level pressure (MSLP) fields and tracks are shown in Fig. 2. The MSLP fields over land, especially over the CMR, are extrapolated from the model-simulated surface pressure fields. Because of the difficulty in estimating the model forecast track after the simulated typhoons have made landfall (Taiwan has more than 100 peaks over 3000 m in the CMR), the model forecast tracks shown in Fig. 2 are estimated based not only on the simulated MSLP but also the simulated upper-level geopotential heights and wind circulation. The simulated typhoon intensities are in very good agreement with observations (especially with those from the Japan Meteorological Agency or JMA best track) after 24 h of model integration[*]. The simulated intensities in the early stages of the model simulations have a low bias due to the fact that no initial bogus vortex is used to spin up the model. The simulations also capture the fact that the typhoon moved slowly and weakened after it made landfall over Taiwan. In general, the simulated tracks match the observed before landfall; however, the track error becomes larger over the high terrain area and after the typhoon re-emerges over the Taiwan Strait. The typhoon also moves out of the 2 km grid domain during the last 12 h of the 72-h integration.

In general, WRF produced the right spatial distribution as well as total amount of precipitation for Morakot (Fig. 3). For example, the main precipitation event is elongated in the southwest-northeast direction and concentrated in a north-south line over southern Taiwan as observed. The
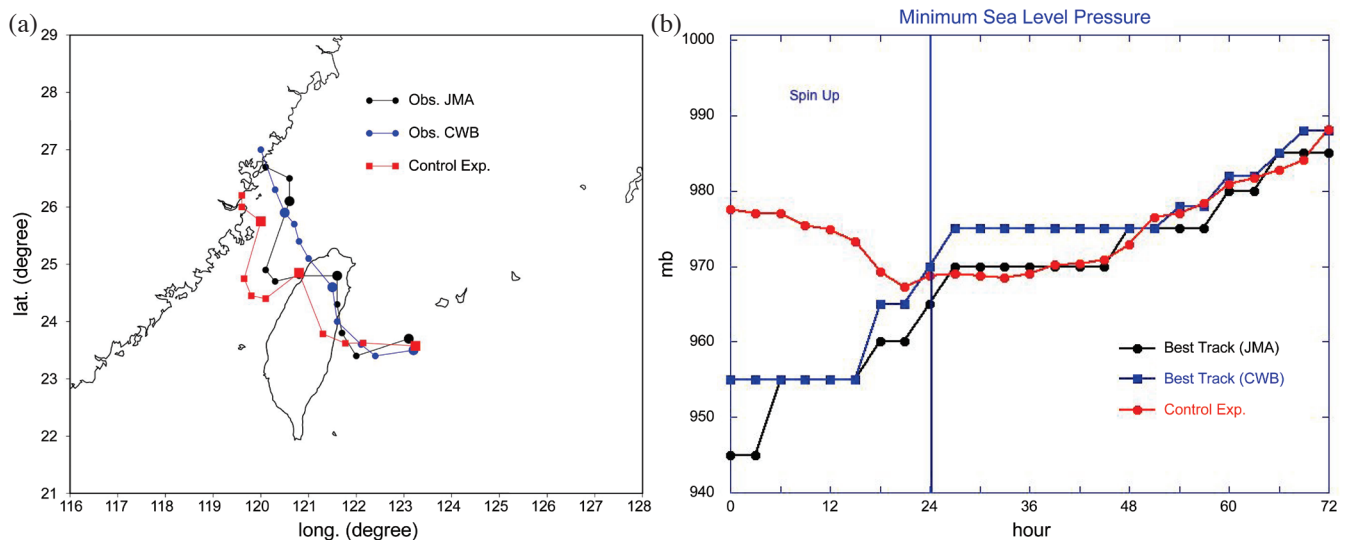

Fig. 2. (a) Corresponding hurricane tracks and (b) minimum sea level pressures (hPa) obtained from WRF forecasts for the Morakot case. The observed track and minimum sea level pressure (solid black line - from JMA) are also shown for comparison.

---

[*] *There are differences in the track (after the typhoon leaves Taiwan) and intensity estimates (about 5 - 10 hPa) between the JMA and Taiwan Central Weather Bureau (CWB).*
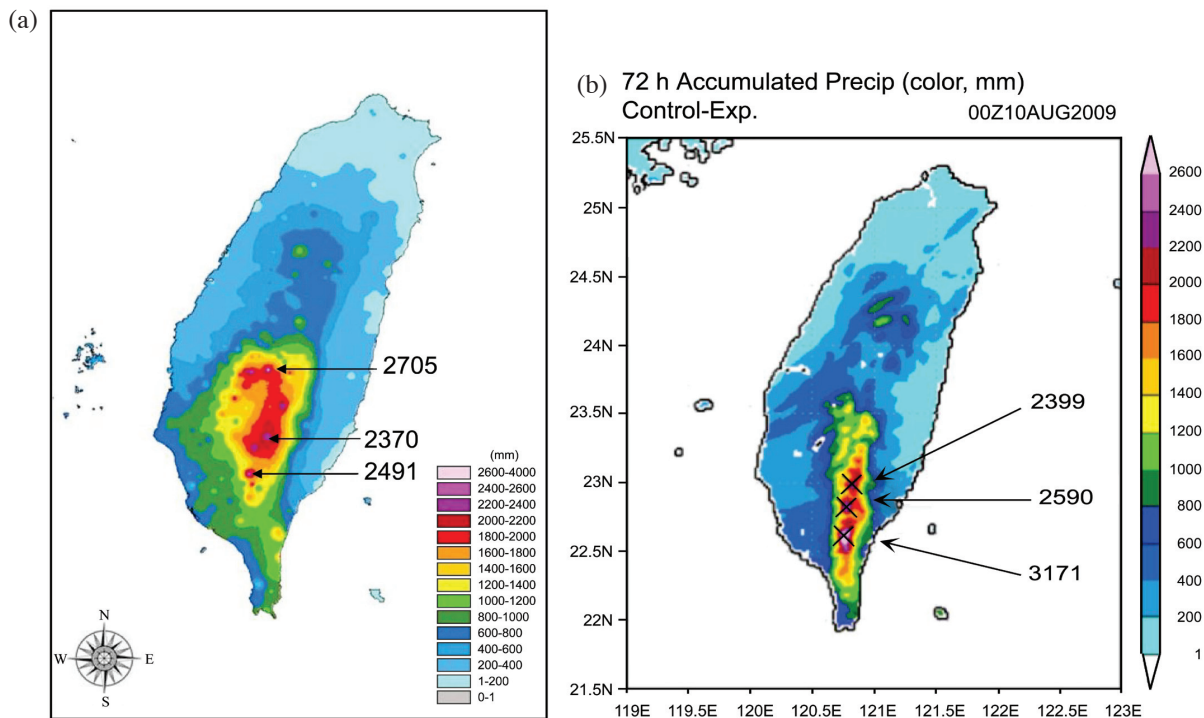
Fig. 3. (a) Observed and (b) model-accumulated rainfall from 0000 UTC 7 August to 0000 UTC 10 August 2009. The numbers in the figure indicate the location and total rainfall amount. The model rainfall accumulations shown in (b) are based on the simulated rainfall in the inner domain (2-km grid spacing). The observed rainfall accumulations are based on the estimate from 394 surface rain gauge stations.

model simulation shows three areas of heavy rainfall over southern Taiwan with the largest maximum located at the southern end of the heavy rain area. The maximum rainfall from the model simulation is over 3100 mm over the 72-h model integration, which is more than the 2700 mm that was observed. One major difference is that the model simulated a heavy rain area (> 1200 mm, shown in yellow in Fig. 3) that is much narrower than was observed. Another difference is that the model-simulated heavy rainfall area seems too far south compared to the observations. The location of the simulated rainfall maximum (3171 mm) is farther south than that of the observed rainfall maximum. This could be due to the fact that the model-simulated track is farther south than was observed. However, the rain gauge network is much denser at lower elevations; therefore, under-sampling could lead to analysis error at higher elevations.

Model accumulated rainfall and rain intensities over five different terrain regions (less than 100 m, 100 - 500 m, 500 - 1500 m, 1500 - 2500 m and higher than 2500 m) are shown in Fig. 4. The results show that most of the surface rainfall occurs over terrain above 1500 m. The results also indicate that rain accumulation and intensity are much weaker over low terrain than they are over high terrain.

Rainfall intensities over moderate (500 - 1500 m) and high terrain (> 1500 m) midway through the simulation are also stronger than during the first and last 24-h periods (Fig. 4b). This suggests that terrain-induced lifting (i.e., upward motion) enhanced the precipitation processes and increased the rain intensities. Furthermore, rain intensities are stronger over the higher terrain regions (Fig. 4b). This suggests that terrain-induced lifting is enhanced over higher elevations. WRF simulates the bulk of the rain between 8 and 9 August (from 24 to 48 h of model integration) as was observed (see Fig. 5).

Previous modeling results (Chiao and Lin 2003; Chen et al. 2007; Yang et al. 2008; Fang et al. 2011; and others) have also suggested that the terrain could enhance precipitation from tropical cyclones. Additional tests reducing the Taiwan terrain height by 25, 50, and 75% reduced the amount of heavy rainfall by 16, 27 and 39%, respectively. Topographic areas seem to be affected more by reductions in the terrain height. This result is generally consistent with Wu et al. (2002), though the terrain effect is not the only factor contributing to the heavy rainfall in this case as heavy rain still occurs even when the terrain height is reduced by 75%*.

---

* More detailed discussions on the impact of Taiwan's topography and model resolution on the simulation of Morakot will be discussed in Part II.

(a) 72 h Average Accum. Rainfall (mm) in Different Terrain Regions Control Exp.

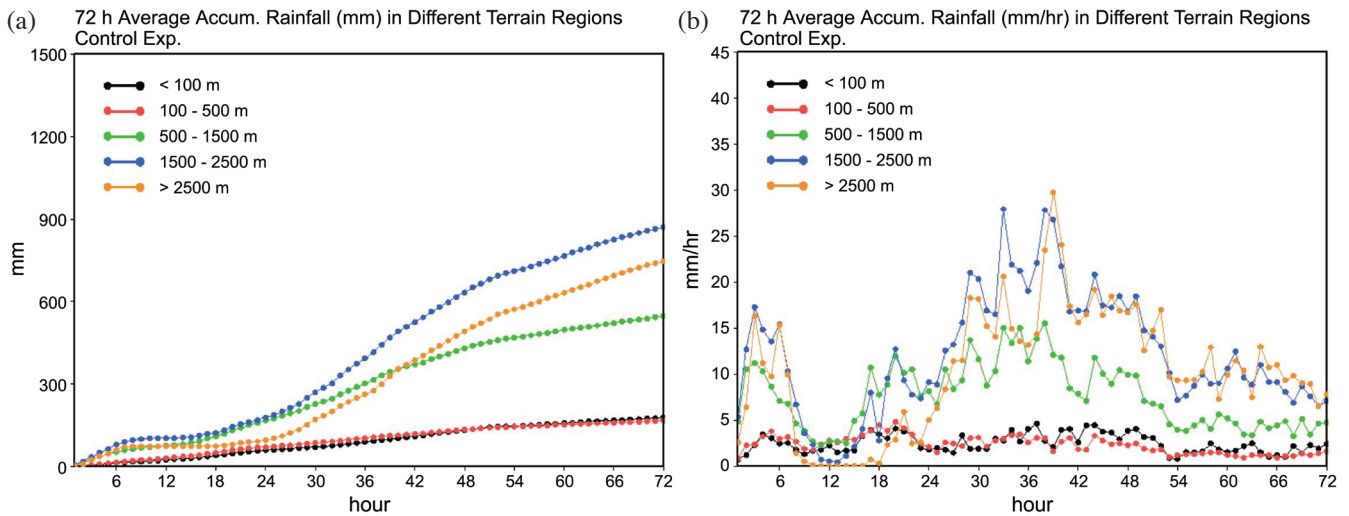(b) 72 h Average Accum. Rainfall (mm/hr) in Different Terrain Regions Control Exp.

Fig. 4. (a) Model accumulated rainfall (hourly) and (b) average rain rates for five different terrain regions (lower than 100 m, 100 - 500 m, 500 - 1500 m, 1500 - 2500 m and higher than 2500 m) from 0000 UTC 7 August to 0000 UTC 10 August 2009. The rainfall and rain rates were produced by grouping 72-h rainfall data from grid points having terrain heights within a specified range (e.g., 500 - 100 m or 500 - 1000 m); average values were computed based on those grid points only.

(a) 72 h Average Rainfall (mm) in Different Terrain Regions

(b) 72 h Average Rainfall (mm/hr) in Different Terrain Regions
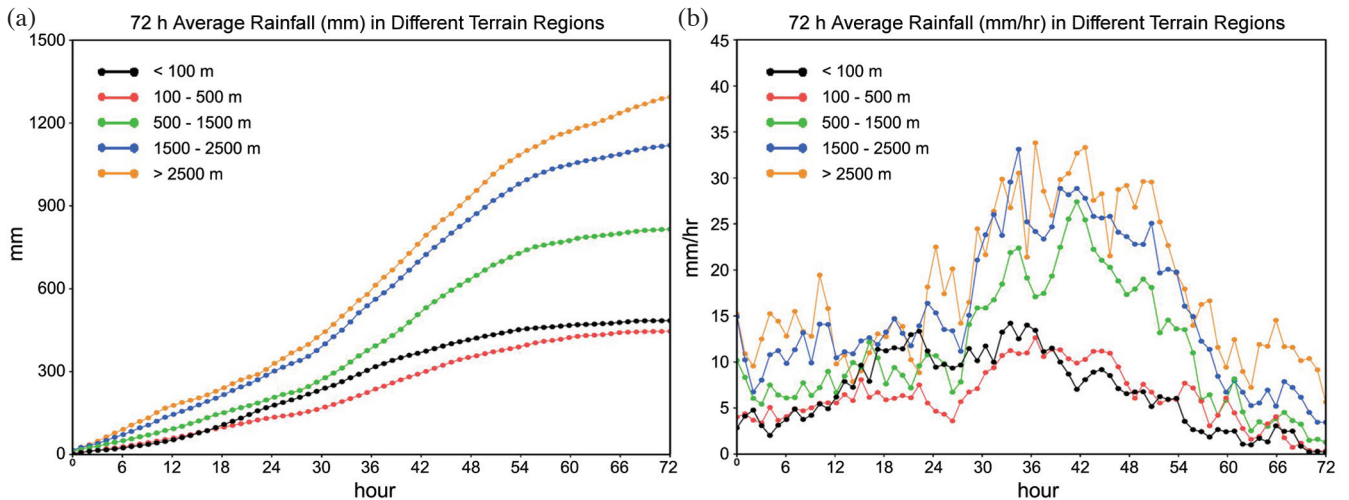
Fig. 5. Same as Fig. 4 except for observed. The rainfall and rain rates were produced in the same way as Fig. 4 except that surface rain gauge data were used instead of the model data.

In order to compare model results with observed rainfall, Fig. 5 shows rain gauge data that has been binned by altitude. The model captured the observed rainfall well in the following ways: (1) more rainfall occurs between 8 and 9 August, (2) rain intensities are stronger over moderate (500 - 1500 m) and high terrain (> 1500 m) regions, (3) they both have very similar rainfall characteristics (intensity and accumulation) over low terrain regions (< 100 m and 100 - 500 m), and (4) the highest rain intensities and accumulation are over high terrain (> 1500 m). There are, however, two noticeable differences: the observed rainfall intensity over low terrain is stronger and more rain is observed over higher terrain (> 2500 m) than in the model.

There are three physical processes responsible for the heavy rainfall over southern Taiwan for this particular case: the typhoon vortex circulation, terrain-induced lifting and the southwesterly flow. The typhoon vortex-induced circulation brings large-scale inflow and its associated upward motion over the western side (or upstream side) of Taiwan. The simulated surface latent heat flux and 900-hPa-level wind after 1, 12, 24, 36, 48 and 60 h of model integration are shown in Fig. 6 to examine the relationships between these three different processes. The surface moisture fluxes are closely tied to the typhoon vortex-induced circulation around Taiwan (Fig. 6b). It appears that the southwesterly flow with its abundant moisture from the South China Sea

and the typhoon-induced large-scale airflow start to merge on 8 August (Figs. 6c and d). However, the southwesterly flow could also be part of the cyclone circulation itself. The 900-hPa-level wind becomes perpendicular to the north-south orientation of Taiwan's terrain (Figs. 6d and e). This would allow terrain-induced lifting to be more effective.

Inert tracer calculations are conducted to examine the impact of the southwesterly flow from the South China Sea and the typhoon-induced circulation on the heavy rain in southern Taiwan. Two tracers are specified southwest and west of Taiwan, respectively (Fig. 7a), and are initialized with a value of one from the surface up to 850 hPa, which
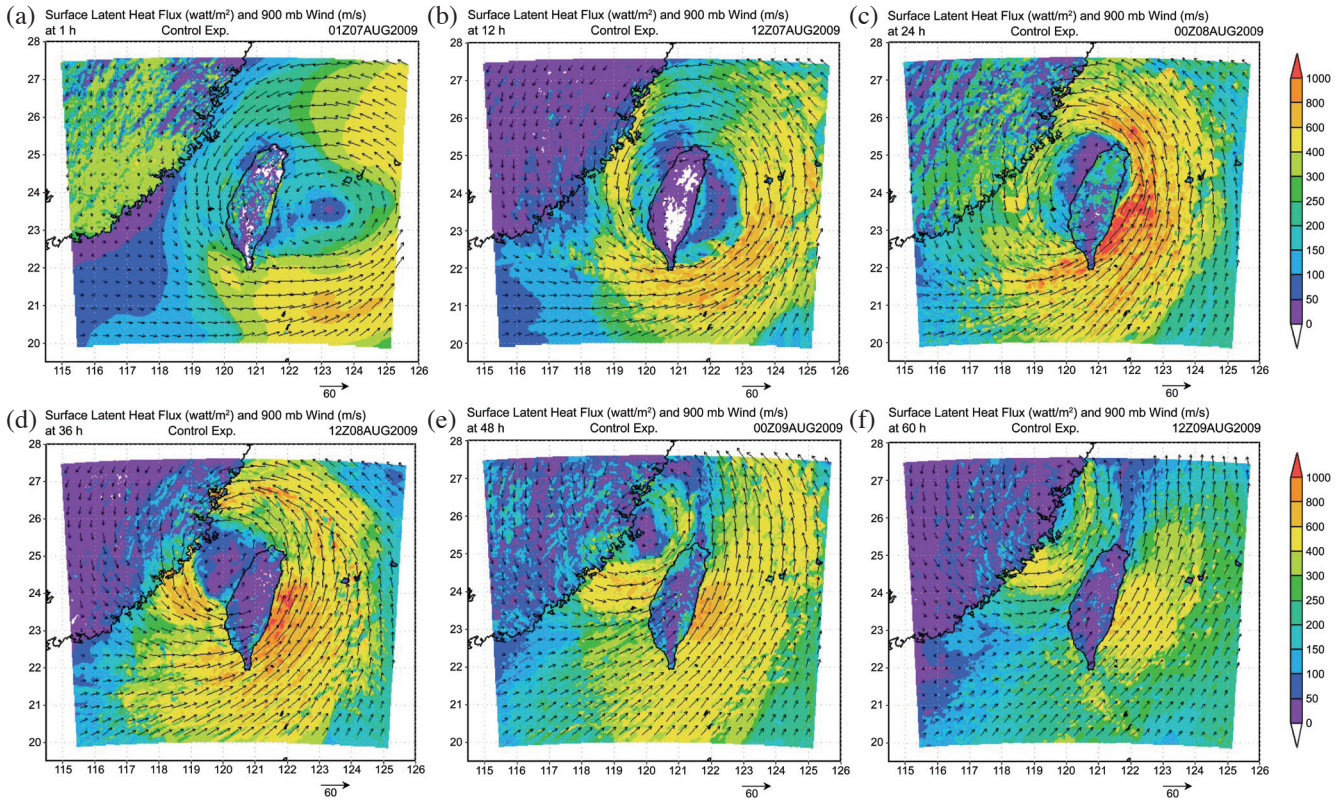

Fig. 6. Simulated surface latent heat flux (W m^{-2}, shaded) and 900 hPa wind (m s^{-1}, vectors) at (a) 1, (b) 12, (c) 24, (d) 36, (e) 48 and (f) 60 hours of integration for the control run.
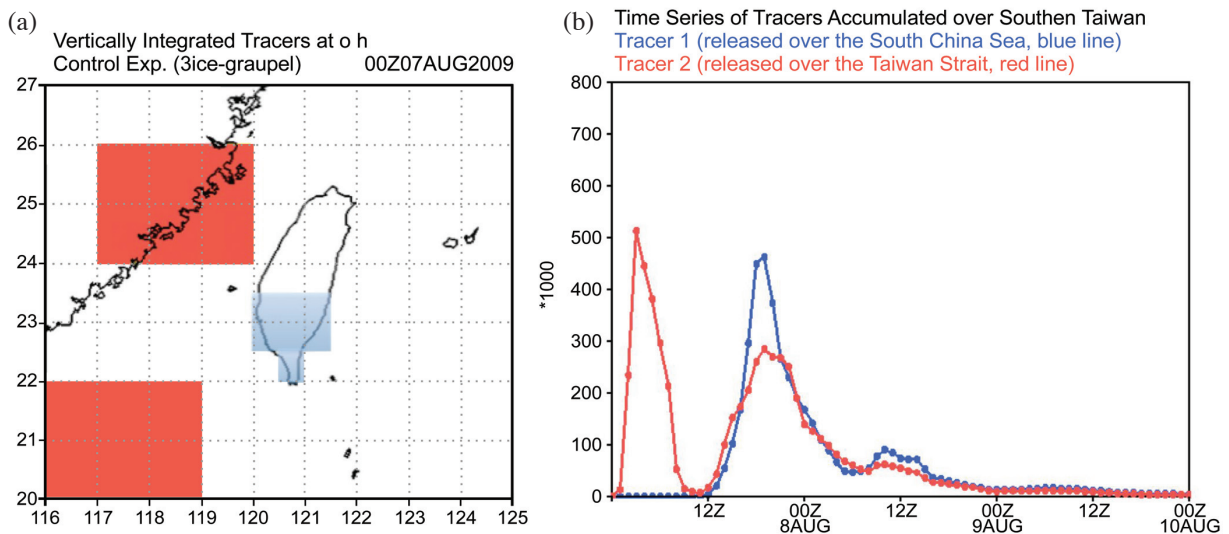

Fig. 7. (a) Geographic locations of the initial inert tracer and (b) temporal- and domain-integrated tracer for the region of Taiwan located south of 23°N where the heavy rain occurred.

spans the layer of abundant moisture. Figure 7b shows the temporal variation of the model-integrated tracer over the region with heavy rainfall. The results show that the southwest flow plays an important role in transporting water vapor into the heavy rain region after the first 12 h of model simulation. However, the tracer results also show that the transport of moisture via the southwesterly flow occurs by way of the typhoon-induced circulation, which actually draws the moisture east of Taiwan before circulating it back towards the west and then over the island. The southwesterly

flow merges with the westerly flow before entering Taiwan from the west (clearly evident in visualization). The model results suggest that the rainfall distribution associated with Morakot is determined by the large-scale circulation pattern (i.e., the typhoon-induced large-scale circulation). The subsequent interaction between the terrain and moisture flux was the dominant factor that led to the devastating floods/landslides.

Figure 8 shows time series of simulated rainfall across three different latitudes, 23.5, 23.0, and 22.5°N, respective-
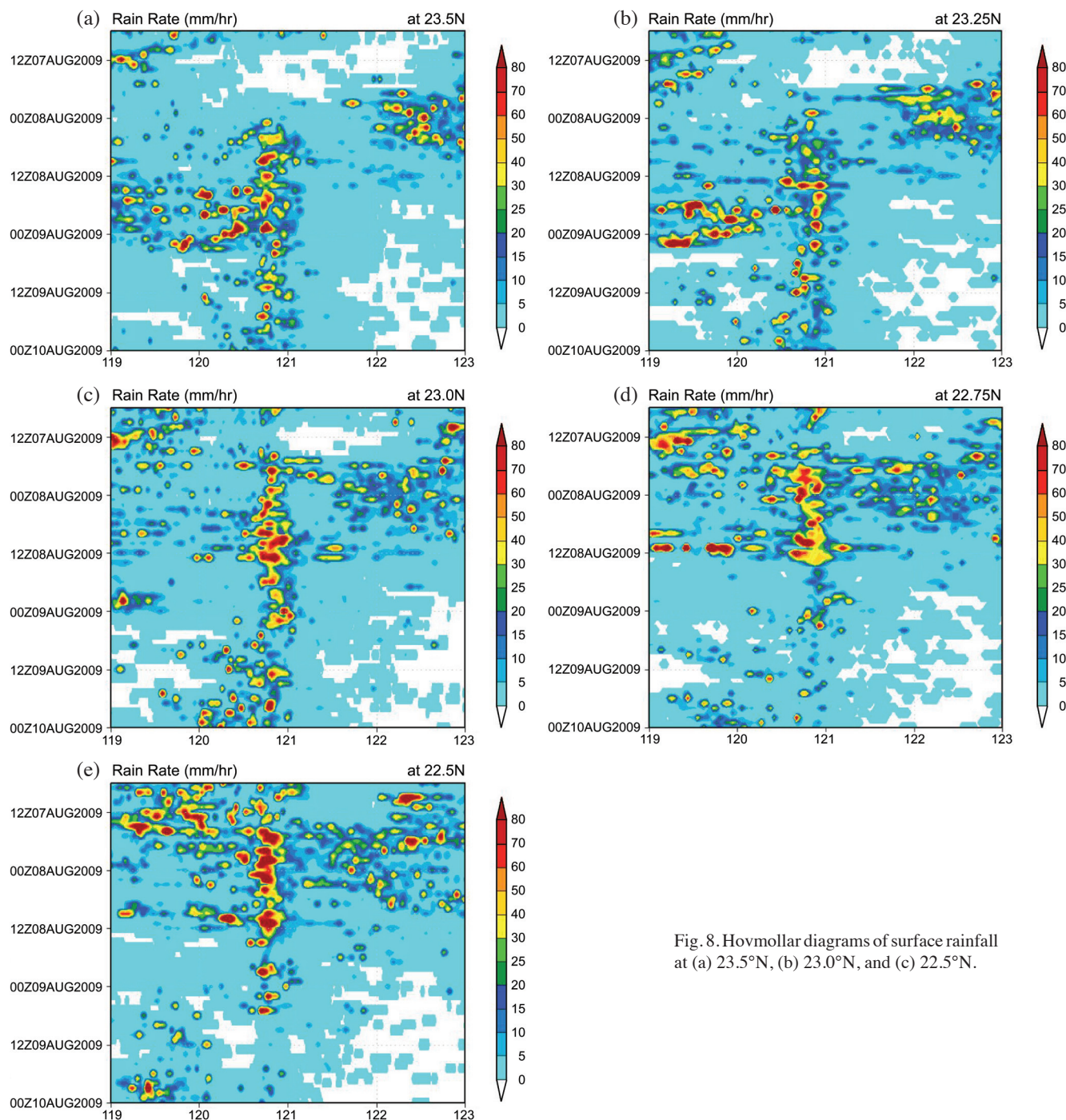

Fig. 8. Hovmollar diagrams of surface rainfall at (a) 23.5°N, (b) 23.0°N, and (c) 22.5°N.

ly. Rain mainly occurs over ocean on both the east and west sides of Taiwan from 0000 UTC 7 August to 0000 UTC 8 August. These areas of rain are mainly associated with the typhoon. After 0000 UTC 8 August, the main areas of rain occur over the west coast and western side of Taiwan. Some of them appear to originate from the Taiwan Strait and propagate over the island of Taiwan. For example, there are rain areas that are originally far from the Taiwan coast (Fig. 8c). These cells are associated with southwesterly flow. In addition, some rain occurs very close to the coast of Taiwan [i.e., from 0000 to 1200 UTC 8 August (Fig. 8a), 0000 UTC 8 August to 1800 UTC 9 August (Fig. 8b) and 1200 UTC 8 August to 0000 UTC 9 August (Fig. 8c)]. Nearly all of the rain areas became stronger or intensified over terrain and was likely caused by terrain effects (i.e., additional lifting).

Time evolution of the model-simulated radar reflectivities and winds along latitude 23°N are shown in Fig. 9. The results indicate that there are several precipitating convective cells (or features) that develop over the Taiwan Strait and then propagate inland. These convective cells become stronger as they near Taiwan. The results also show that enhanced upward motion occurs when the precipitation systems move closer to and over terrain (> 1000 m, see Fig. 9b). Higher reflectivities occur when the cells reach even higher terrain (Figs. 9d and e). Strong radar reflectivities (approaching 40 dBZ) reach nearly 8 km and are in good agreement with observations (Fig. 10, from Jou et al. 2010).

Also, the reflectivities in the observed rainbands over the southern Taiwan Strait (Fig. 10) do not show evidence of a bright band. These observations indicate that the precipitation processes associated with the rainbands are warm rain dominated. In addition, the highest reflectivities (> 50 dBZ) are limited to 5 km or lower, which is also in good agreement with observations. This suggests that warm rain processes dominate the heavy precipitation in this case.

5. SENSITIVITY OF MICROPHYSICS AND PBL SCHEMES

5.1 Microphysics

Two sensitivity tests on the microphysics (improved and warm rain only) are conducted. The observed and simulated MSLP fields and tracks for the control and these two tests are shown in Fig. 11. The improved microphysics does not improve the track forecast. Its predicted track is slower before the cyclone moves over the Taiwan Strait than the control case. The simulated track is also too far south compared to the observed track but is slightly better than the control case. On the other hand, the improved microphysics results in a stronger simulated MSLP after 12 h of model integration than the control case. This feature is in better agreement with observations, but later the scheme produces a stronger intensity (by about 15 hPa) than the control case and observations.
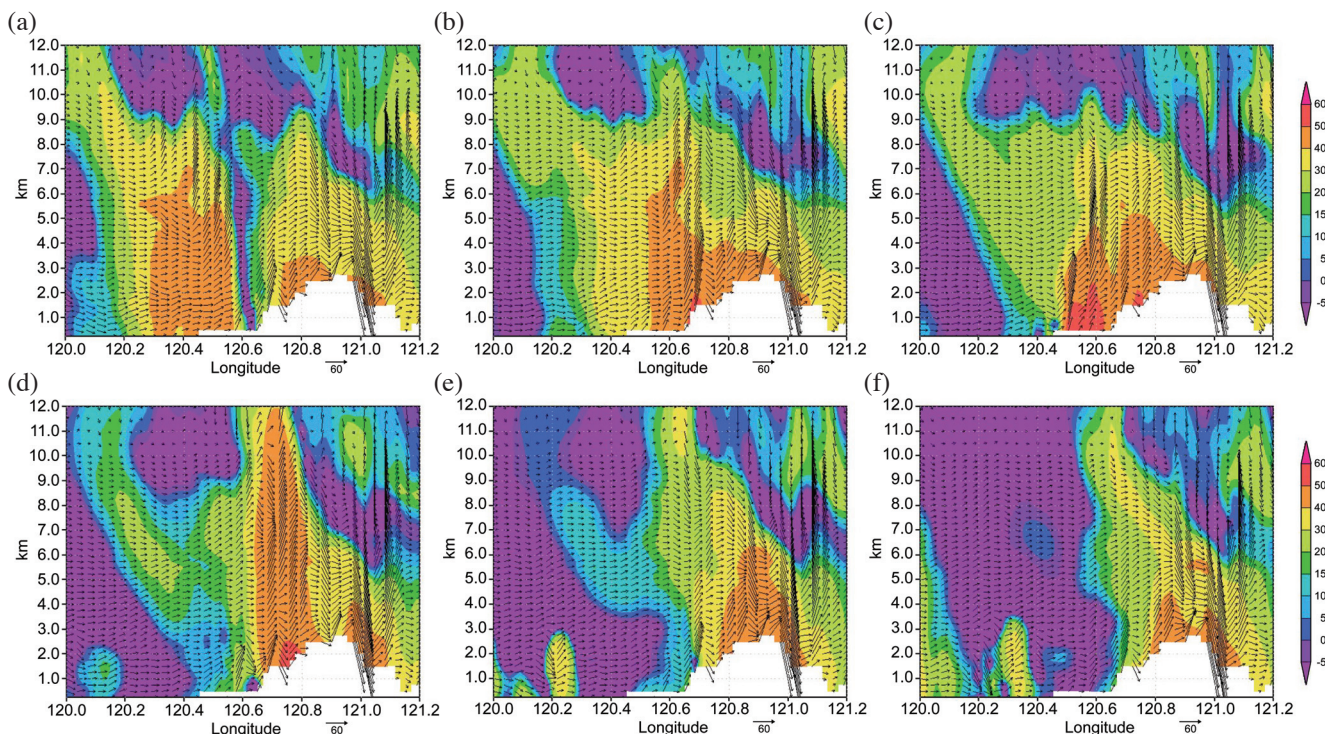

Fig. 9. Simulated radar reflectivity (dBZ, shaded) and wind (m s^{-1}, vectors) at 23.0°N at (a) 1550 UTC, (b) 1600 UTC, (c) 1610 UTC, (d) 1620 UTC, (e) 1630 UTC and (f) 1640 UTC on 8 August 2009.
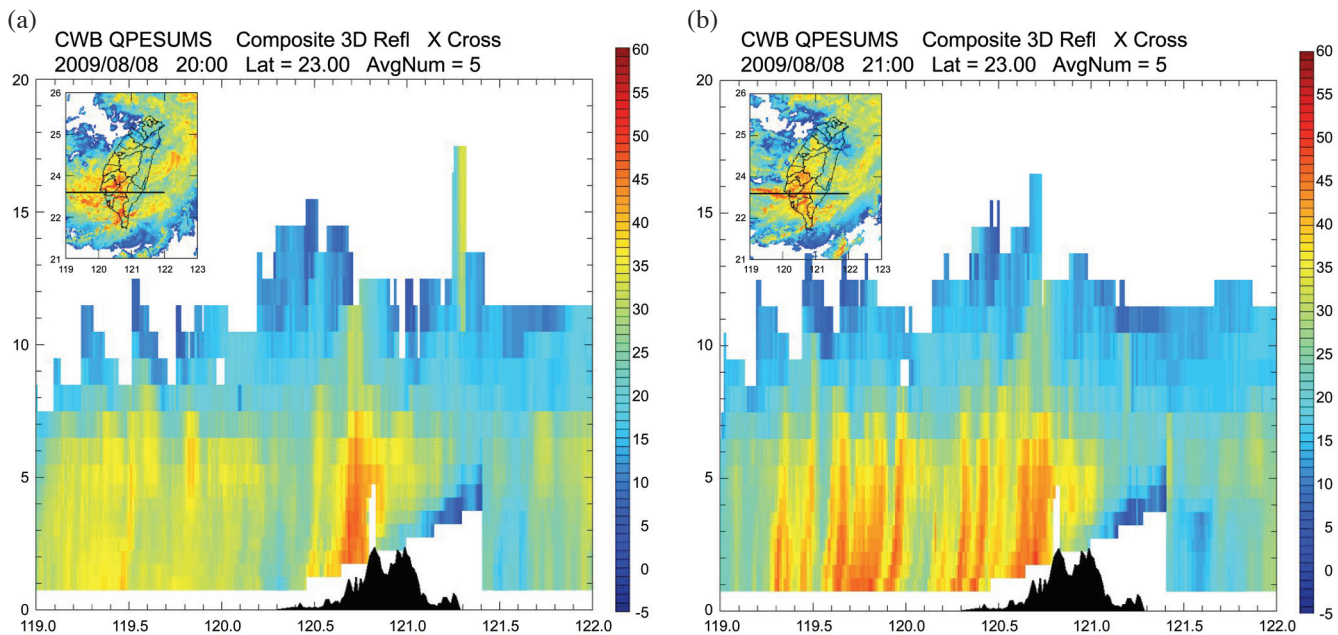
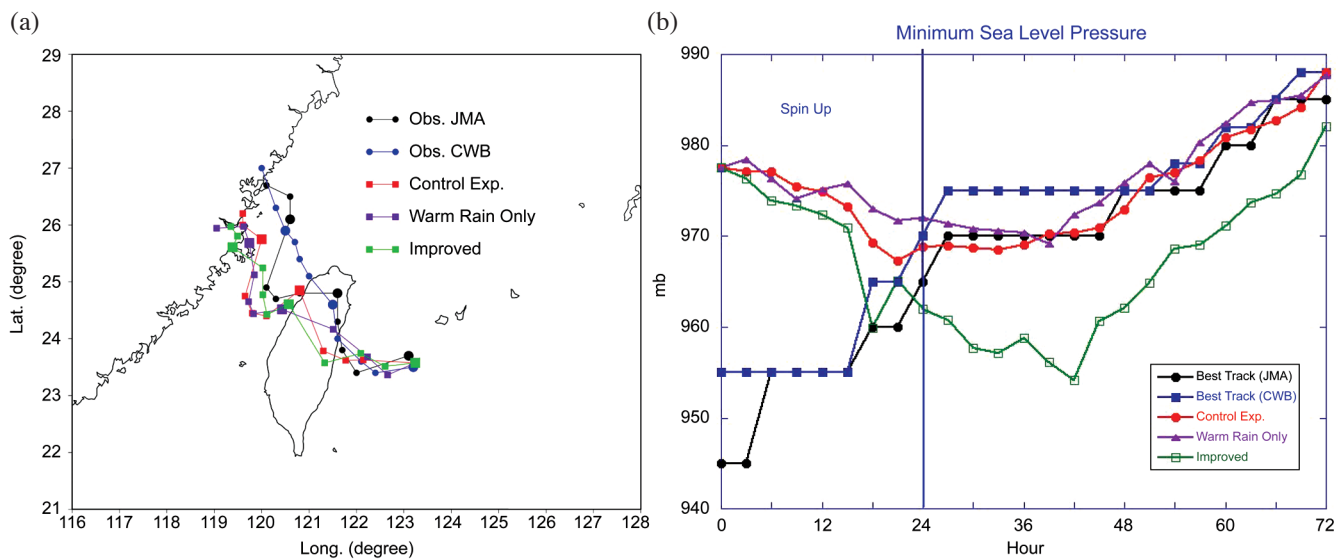Fig. 10. Observed radar reflectivity (dBZ) at 23.0°N at (a) 2000 UTC and (b) 2100 UTC on 8 August 2009.

Fig. 11. Same as Fig. 2 except for the simulations with improved microphysics and warm rain only.

For the warm rain case, the simulated track and intensity are similar to the control case, which actually disagrees with previous research. Nearly all of the previous studies found that simulated hurricanes, including a previous Hurricane Katrina (2005) simulation, had the strongest deepening or intensification when using only warm rain physics (Tao et al. 2011). This is because all of the simulated precipitating hydrometeors are large raindrops that quickly fall out near the eye-wall region, which would hydrostatically produce the lowest pressure (Wang 2002; Yang and Ching 2005).

A possible reason for this contradiction is the dominance of warm-rain processes in Morakot, which is different from many other storms. For example, Table 2 gives the relative fraction of liquid (cloud water and rain) and solid (cloud ice, snow and graupel) water contents based on time-domain averages for Katrina and Morakot. More than two thirds of the cloud species in Katrina were ice. This is because Katrina had stronger deep convection, which lofted more ice particles aloft, than did Morakot. As opposed to Katrina, there were more liquid than solid hydrometeors over

the region of heavy rainfall in Morakot (the third column in Table 2). Furthermore, Fig. 12 shows cross sections of the 24-hour accumulated liquid/ice particles from the control and improved 3ICE experiment. More ice species are present aloft (above 400 hPa) after 24 h model integration for the improved case. This is due to the fact that the improved scheme produces more cloud ice; it also produced a stronger storm. In addition, much more warm rain is clearly present in the Morakot case. Warm rain is especially dominant from 24 to 48 h of model integration when the heavy rainfall occurs (Fig. 4). This could explain the similarity between the control and warm rain cases.

The observed and WRF-simulated rainfall using the Goddard improved microphysics scheme (Lang et al. 2011) and warm rain only are shown in Fig. 13. Generally speaking, WRF produced the right distribution of precipitation despite using two different ice microphysical options (the control run is shown in Fig. 2b). All options resulted in simulations wherein the main area of precipitation continued over southern Taiwan over a 72-h period. All runs produced

Table 2. Domain- and 72-h time-average accumulated liquid (warm rain) and solid (ice) water species for the Katrina and Morakot cases. The time-average is based on 72, hourly data outputs. The third column shows the region where heavy rainfall occurred.

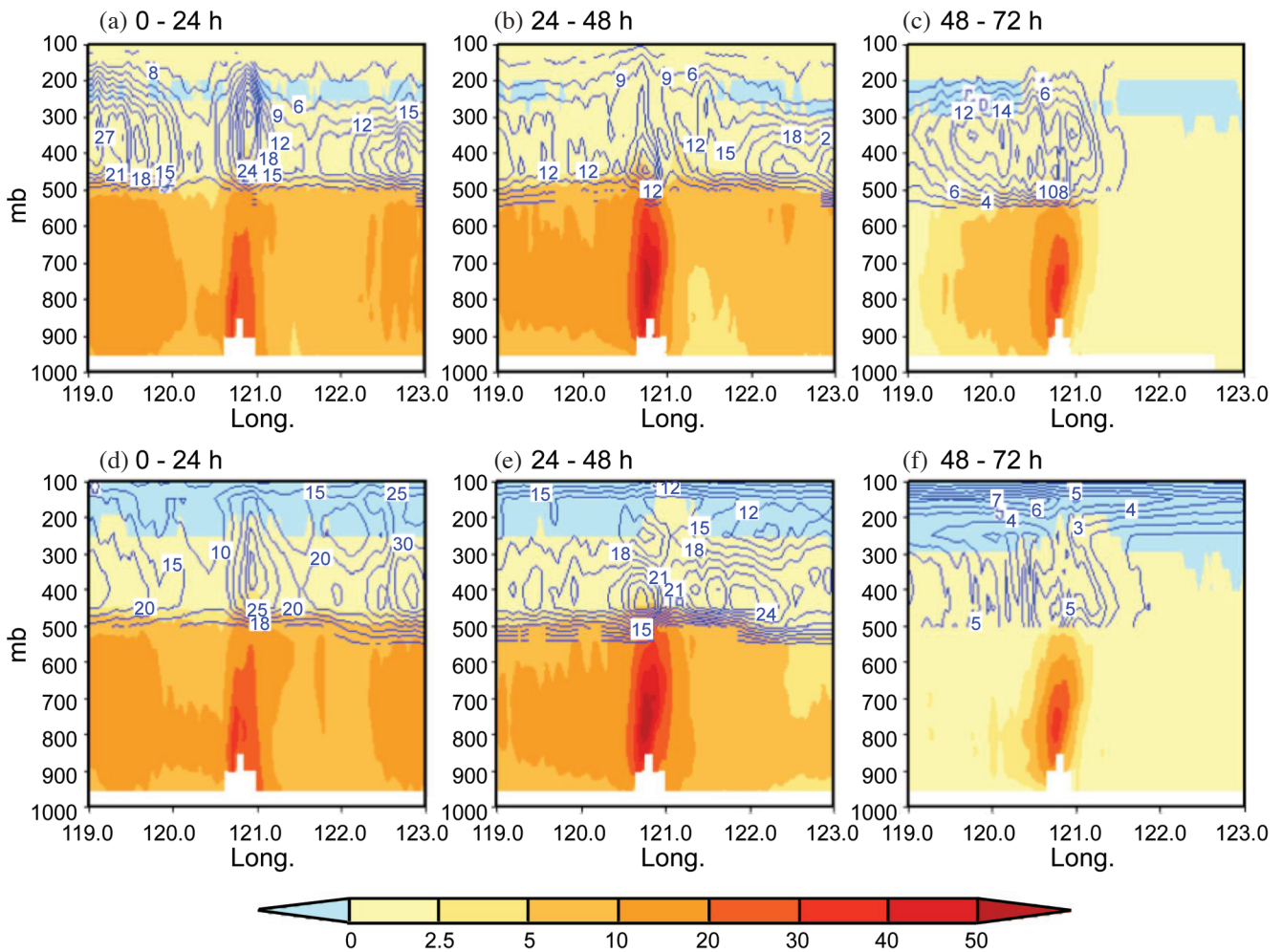|	Katrina	Morakot	S. Taiwan below 23.5°N
Liquid hydrometeor	36.4%	43.64%	51.75%
Solid Hydrometeor	63.6%	56.36%	48.25%

Fig. 12. Cross section of accumulated liquid/ice (g kg^{-1}) for the (a) 1st, (b) 2nd and (c) 3rd day of the simulation from the control experiment. The color-shaded area represents the warm rain (cloud water and rain) and the contours represent the ice (cloud ice, snow and graupel). (d), (e) and (f) are the same as (a), (b) and (c) except for the improved ice scheme.
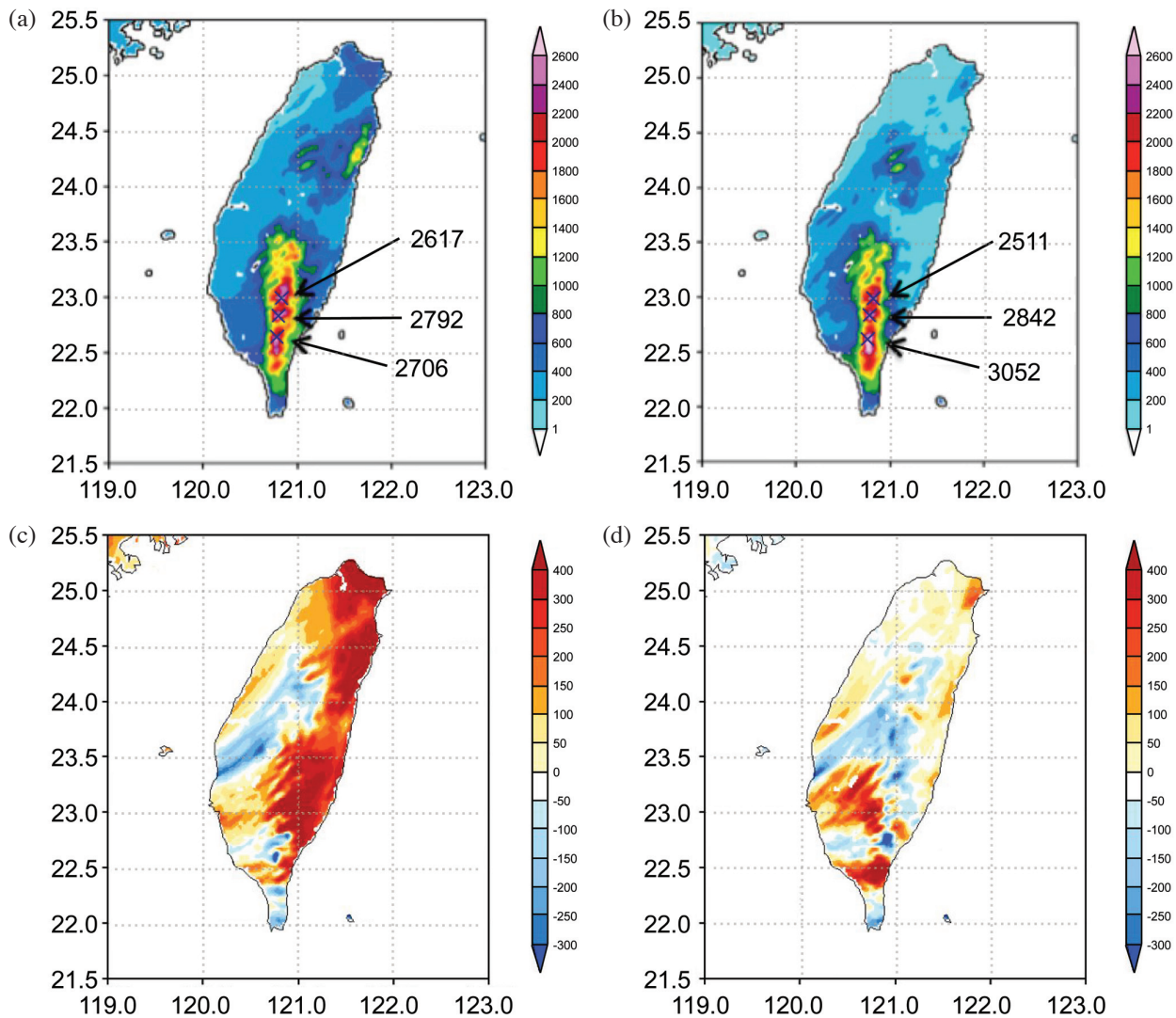
Fig. 13. (a) Improved and (b) warm rain only model accumulated rainfall from 0000 UTC 7 August to 0000 UTC 10 August 2009. (c) is the difference between the improved and original microphysics and (d) is the difference between the warm rain and original microphysics.

more than 2700 mm of rainfall over southern Taiwan. The improved 3ICE-graupel produced a lower maximum (2792 mm in Fig. 13a), which is in better agreement with observations than the control case (see Fig. 2a). The warm rain only case also produces results that are similar to the two 3ICE schemes in terms of rainfall pattern with the maximum rainfall over south Taiwan. Interestingly, the warm rain case produced a higher rainfall maximum (over 3000 mm; see Fig. 13b) compared to the improved 3ICE scheme and as much as the control case. These results again suggest that warm rain processes are the dominant precipitation processes.

Differences in rainfall between the control and sensitivity cases (Fig. 13) appear to be a result of differing fall speeds between the microphysics options. For example, with the improved microphysics more rainfall is simulated over the east coast and northern part of Taiwan due to having a greater abundance of smaller ice particles (cloud ice) and/or snow. This is the main characteristic of the improved microphysics (Lang et al. 2011). The fall speed for snow and cloud ice is slower than graupel, which results in more precipitating ice particles (i.e., cloud ice and snow) reaching high terrain regions and falling over eastern Taiwan. Consequently, more precipitating ice particles can reach the high terrain region as well as flow/move over the terrain ridge and fall on the east coast side of Taiwan. On the other hand, less rain is simulated over southern Taiwan (within the southwest flow) and over lower terrain regions as slow-falling snow particles are carried farther downstream. Overall more rain is simulated over Taiwan for the improved case, but less rain is simulated over the ocean. For the warm rain case, in general, more rain is simulated along the coast and less is over higher terrain compared to the control case. It should be expected that more rain would be simulated over

the west coast of Taiwan because of the faster fall speed of raindrops, which allows them to fallout and reach the surface sooner. The differences between the control and warm rain case are much smaller than they are between the two ice cases (Fig. 13a).

Overall, the improved microphysics results in more total rainfall over Taiwan than either the control or warm rain cases. Over higher terrain, the higher rainfall totals using the improved physics are in better agreement with observations. At lower elevations (i.e., lower then 500 m), all of the schemes produce similar average rain accumulations of about 200 mm or less (Figs. 4, 14, 15), which is roughly half of what was observed (Fig. 5). Over higher terrain, however, (i.e., above 1500 m) the improved microphysics produces much more rain (on the order of 1000 mm) than either

the control (~700 to 800 mm) or the warm rain run (~600 to 800 mm) physics, which is much closer to the observed values (~1100 to 1300 mm) at those elevations. The improved physics also does a little better at midlevels (i.e., 500 to 1500 m). Accumulated rainfall values in that region for the improved, control and warm rain runs are just over 600 mm, ~500 mm, and just under 600 mm, respectively, whereas the observed value is ~800 mm. In terms of peak rain intensities over higher elevations, the control and warm rain runs are too low while the improved physics is too high; all of the schemes are too low at lower elevations. In addition to the direct effects from the microphysics, the stronger simulated storm intensity (Fig. 11) in the improved case could indirectly lead to more rainfall and higher rain intensities via a stronger cyclone circulation interacting with the terrain.
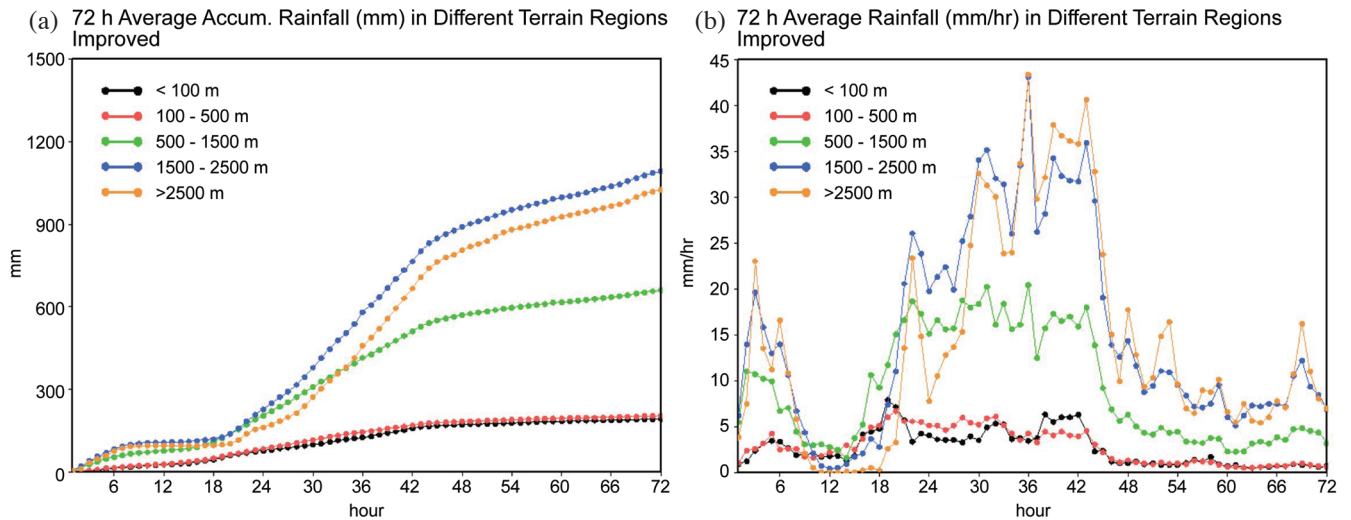

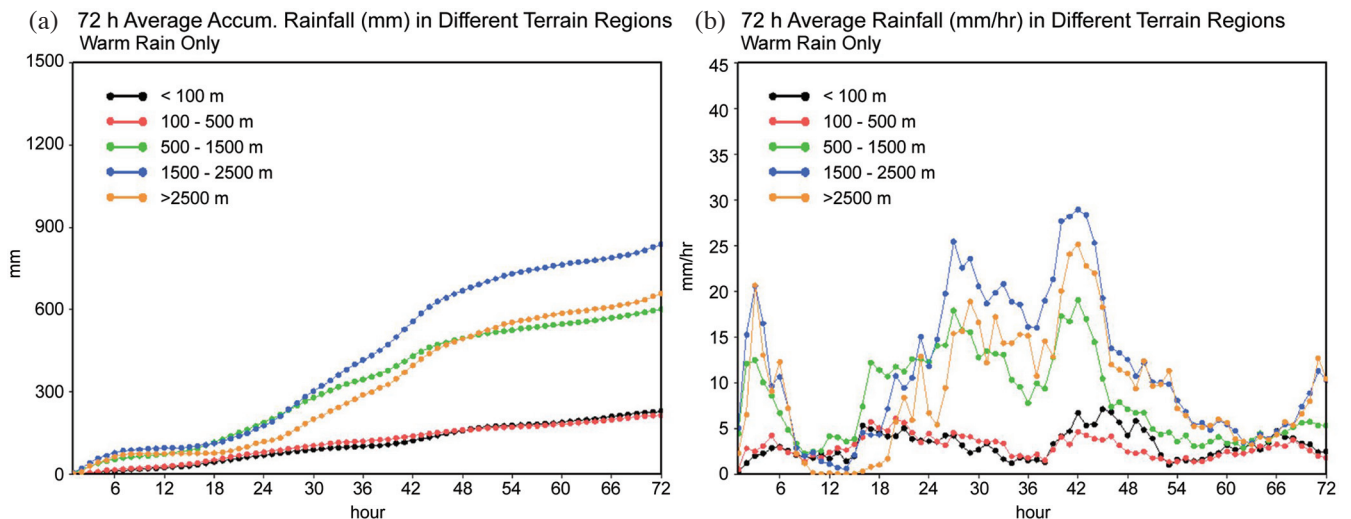Fig. 14. Same as Fig. 4 except for the improved microphysics case.

Fig. 15. Same as Fig. 4 except for the warm rain case.

In contrast to other cases (e.g., South American and West Pacific convective systems; see Lang et al. 2011), the improved mircophysics does not significantly improve the simulation of Morakot. Though the simulation produced a slightly better storm intensity during the first 24 h (Fig. 11) and slightly improved rainfall totals (Fig. 14), it later simulated a typhoon that was considerably stronger than that observed. Another way of looking at the error in rainfall prediction is through the bias and root mean square error RMSE), which are shown in Table 3. The results show that both cases have very similar RMSE. The new microphysics has a better bias though. The large bias and RMSE for both cases is due to the model-simulated heavy rainfall locations not being in the same locations as estimated by the rain gauge network.

It appears that the strong storm in the improved scheme is a result of less evaporative cooling, which leads to weaker downdrafts. Figure 16 shows the simulated mean vertical heating profiles due to the evaporative cooling of cloud and the melting of snow and graupel from the control and improved microphysical schemes. These cooling rates are computed over the first 24 h of model integration when the difference in MSLP appears between the two cases. The results show that evaporative cooling from cloud droplets is stronger by about 0.2°C h^{-1} on average for the control. The melting of precipitating ice is also slightly larger for the control case. This is consistent with Wang (2002) and Zhu and Zhang (2006), who suggested that simulated hurricanes become unrealistically strong when the evaporative cooling of cloud droplets and melting of ice particles are removed. Downdrafts are mainly initiated and maintained by cooling and melting. Consequently, simulated downdrafts are weaker for the improved case due predominantly to weaker cooling from cloud evaporation with less impact from the change in melting. Since downdrafts are mainly initiated and maintained by cooling and melting, simulated

downdrafts in the improved case are weaker, and low-level theta-e is higher (not shown). This ultimately has a positive impact on intensity (Willoughby et al. 1984; Wang 2002).

Vertical profiles of the domain and time average cloud species (i.e., cloud water, rain, cloud ice, snow and graupel) for the improved and warm rain runs are shown in Fig. 17. The improved microphysics produces less graupel than the control run. Snow is the dominant species at midlevels, while cloud ice is the largest at upper levels for the improved case. Although there were no modifications made to the warm rain physics, the modified scheme does lead to smaller cloud water at lower levels. These results are in good agreement with Lang et al. (2011). Also, the total domain-integrated warm rain (cloud water and rain) is about the same as the corresponding ice (cloud ice, snow and graupel). This result is different from the Hurricane Katrina (2005) simulation (Tao et al. 2011) where more than two thirds of the cloud species were from ice. The vertical rain profile for the warm rain case is similar but slightly less than the control and improved microphysics cases below the melting level (550 hPa level); its simulated cloud profile is similar to the control case at low-levels.

5.2 PBL Schemes

Generally speaking, the YSU scheme is a "non-local K" scheme with stronger vertical mixing within the PBL, and the MYJ scheme is a "local K" scheme with relatively

Table 3. RMSE (root mean square error) and bias for the original and improved microphysics.

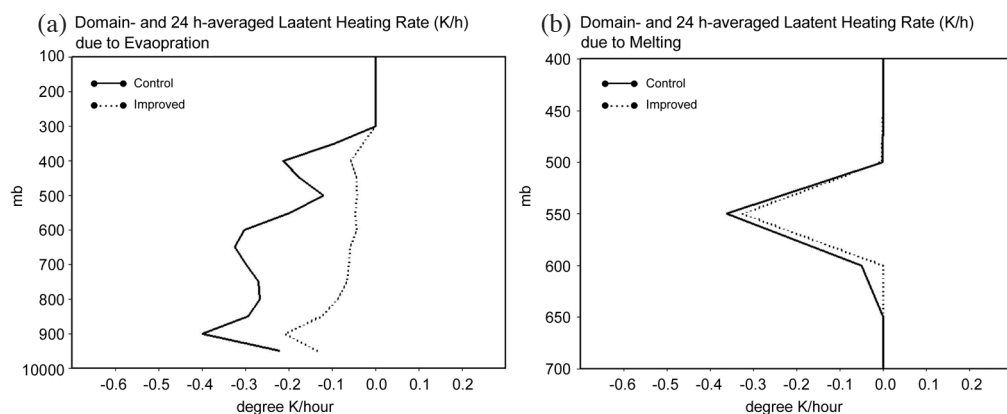|	BIAS	RMSE
Control Exp. (S. Taiwan below 23.5°N)	-422.50	589.08
New (S. Taiwan below 23.5°N)	-330.86	562.45

Fig. 16. Vertical profiles of domain- and time-averaged (0 - 24 h) (a) evaporative cooling, and (b) melting rate from the control and improved microphysics schemes. The domain average covers every grid point in the third domain (538 × 439 grid points). The time step for computing the heating is 2 seconds (in line).

weaker vertical mixing. The detailed differences between the two PBL schemes are described in Appendix B. Figure 18 shows the observed and simulated MSLP fields and tracks for the two different PBL schemes: MYJ (or control case) and YSU. The results show very similar patterns in terms of MSLP (and intensity). The YSU PBL scheme does not improve the track forecast (Fig. 18a). Its predicted track is also very similar to the control case before the cyclone moves to the Taiwan Strait, indicating that the interactions between the PBL processes and Taiwan's terrain produce larger track variations after the cyclone/storm leaves Taiwan. The simulated track is also too far south compared to the observed track. In addition, the YSU PBL scheme simulates more than 2500 mm of accumulated rainfall over southern Taiwan, as did the MYJ scheme (Fig. 19a). Its simulated rainfall pattern is also in good agreement with observations as with the other cases. Despite its similarities with the control experiment, the simulation with YSU simulates more rainfall over the west coast of Taiwan (Fig. 19b),

which can be attributed to higher surface fluxes over the Taiwan Strait. On average, the YSU PBL scheme simulates 50 W m^{-2} more surface latent heat fluxes over ocean than the MYJ scheme (Fig 20a).

However, the YSU scheme simulates more rainfall over the west coast of southern Taiwan (between 22.5 and 23°N, see Fig. 19b). Note that the latent heat fluxes over land are similar between the two schemes. Both schemes also show a strong diurnal variation in surface fluxes over land (Fig. 20b). These results suggest that the stronger surface latent heat fluxes over ocean (where convective cells were initiated before propagating over Taiwan to produce heavy rainfall) could be the reason why the YSU scheme led to more precipitation for this case. Therefore, the surface processes could not explain the stronger intensity simulated by the improved microphysics. Rather, less (or weaker) evaporative cooling (shown in Fig. 16) is more likely the reason for the stronger intensity simulated by the improved microphysical scheme.
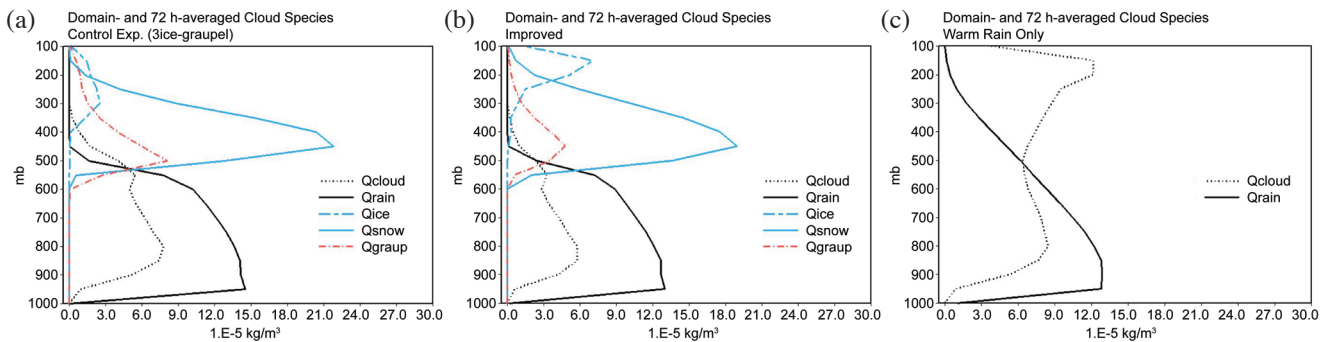

Fig. 17. Vertical profiles of domain- and 72-hour time-average cloud species (i.e., cloud water, rain, cloud ice, snow and graupel) for the (a) control, (b) improved, and (c) warm rain only microphysics.
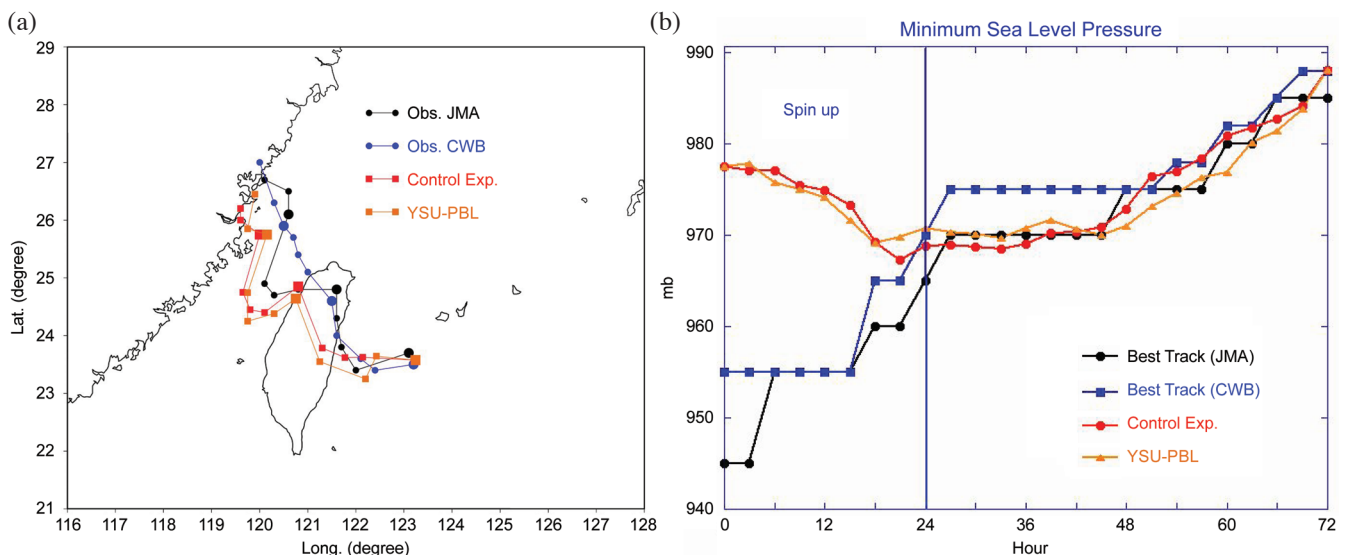

Fig. 18. Same as Fig. 2 except for the simulations with the YSU PBL scheme.
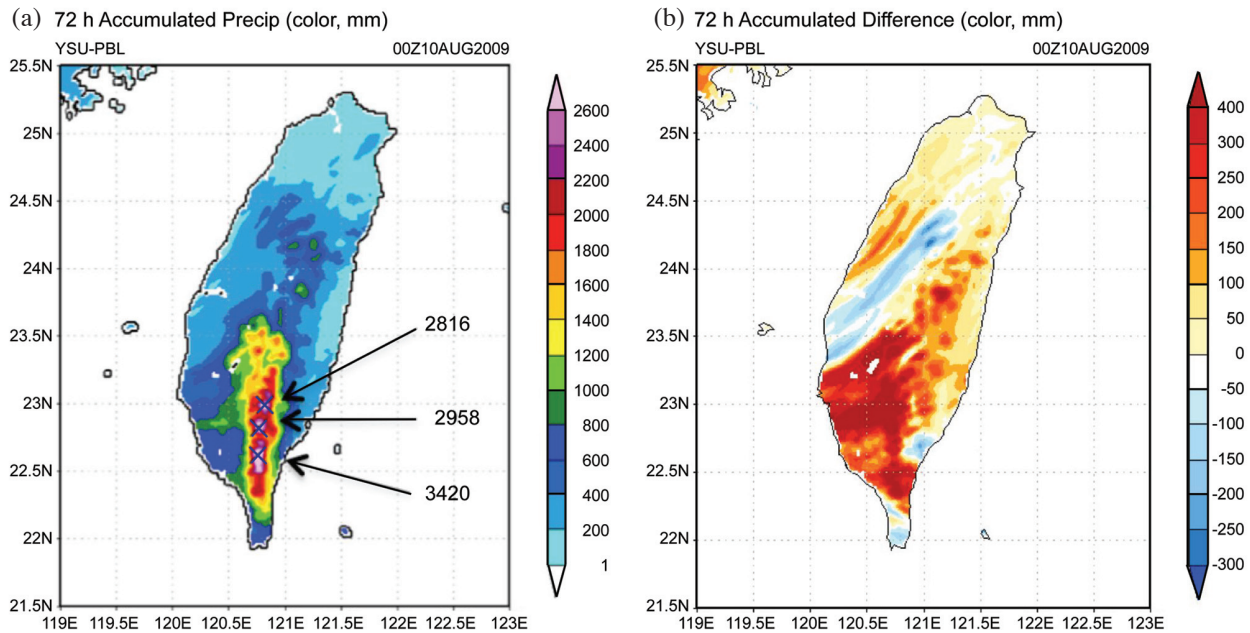
Fig. 19. (a) Model accumulated rainfall for the YSU PBL scheme from 0000 UTC 7 August to 0000 UTC 10 August 2009; (b) the difference between the YSU and MYJ PBL schemes.
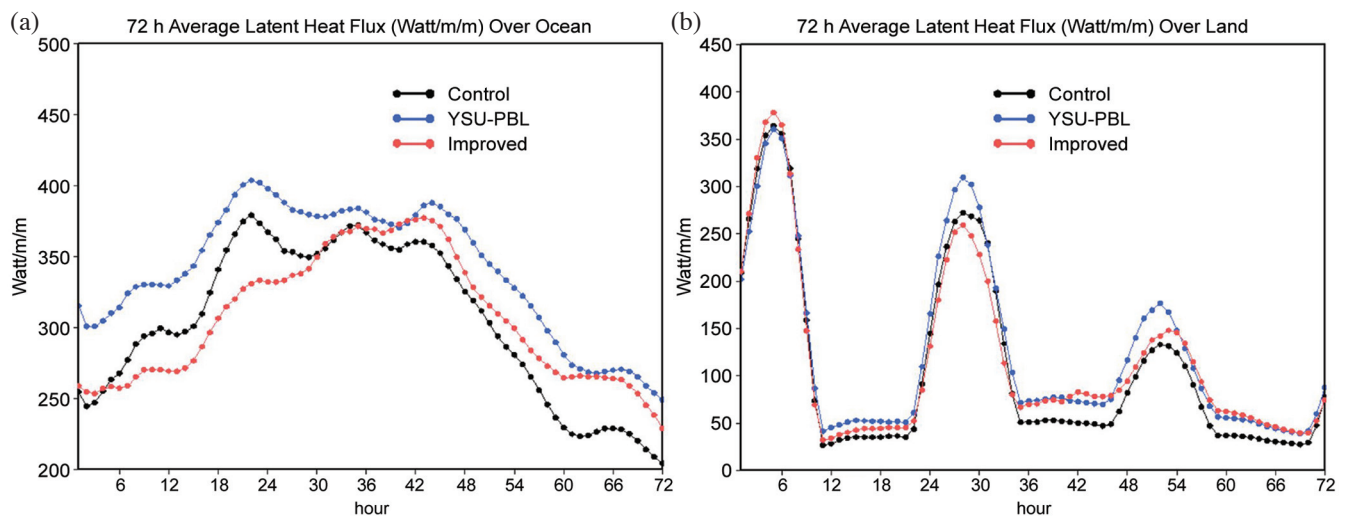

Fig. 20. Time series of domain-averaged latent heat fluxes over (a) the ocean and (b) land for the control, improved microphysics and YSU PBL cases.

Overall, the sensitivity of the simulations to the PBL scheme in terms of track, intensity, total precipitation amount, and rainfall pattern is less than it is with using the two different ice microphysical schemes (control vs. improved microphysics). These results suggest that the role of the PBL process is secondary for this case since heavy precipitation is more organized and largely determined by the large-scale circulation and terrain forcing.

These results are very different from some of the previous modeling studies on the sensitivity of hurricanes to PBL schemes (Braun and Tao 2000; Yang and Ching 2005; Li

and Pu 2008; Nolan et al. 2009a, b; Shin and Hong 2009). For example, Yang and Ching (2005) compared the performance of different PBL schemes for Typhoon Toraji, which made landfall in Taiwan in about the same vicinity, and found that the MRF PBL scheme (an old version of the YSU) produced a simulated track and intensity that most resembled the observations. Different size circulations (Morakot had a much larger vortex circulation versus the more compact Toraji) and different synoptic environments (strong southwesterly flow associated with the landfall of Morakot versus much weaker southwesterly flow for Toraji)

may explain the different responses in the PBL sensitivity experiments. Shin and Hong (2009) also used the WRF with 3 km grid spacing to simulate the heavy rainfall associated with Typhoon Nari (2007) over Jeju Island, South Korea. Their results showed that the YSU PBL scheme simulated almost twice as much rainfall as the MYJ scheme in better agreement with observations. On the other hand, Li and Pu (2008) and Nolan et al. (2009a, b) showed that the MYJ scheme produced a stronger storm in better agreement with observations of Atlantic systems. Li and Pu (2008) showed that the MYJ PBL scheme has a larger and more rapid increase in surface latent heat fluxes than the YSU scheme. The different conclusions from the Atlantic [Hurricane Bob (1991) in Braun and Tao 2000; Hurricane Emily (2003) in Li and Pu 2008; and Hurricane Isabel (2005) in Nolan et al. 2009a, b] and Pacific [Typhoon Toraji (2001) in Yang and Ching 2005; and Typhoon Nari (2007) in Shin and Hong 2009] storm simulations could be due to the fact that different thermodynamic, stability and moisture conditions exist between the Atlantic and Pacific storm environments, and that the YSU PBL scheme has been widely evaluated and adjusted for the East Asian summer monsoon system (Yhang and Hong 2008).

Typical differences between the MYJ and YSU schemes include the YSU scheme inducing precipitation later in the day with more intensity. At nighttime, stable mixing is stronger in the YSU scheme, which could initiate precipitation earlier. Enhanced mixing in the YSU scheme in general could produce stronger low-level inflow, more inward moisture transport from the environment, and thereby increase precipitation. However, more observational data on the marine PBL characteristics over the Pacific from future field experiments are required to calibrate and evaluate the systematic differences between the YSU and MYJ schemes for typhoon simulations in East Asia.

6. SUMMARY

WRF was used at high-resolution (2-km horizontal grid spacing) to both simulate the heavy rainfall associated with Typhoon Morakot (2009) and to conduct sensitivity tests on the impact of microphysics schemes and PBL schemes on the heavy rainfall for this case. The model results are also compared with those from previous modeling studies to assess the impact of microphysics and PBL schemes on hurricane track and intensity. The major highlights are as follows:

1. The results indicate that the high-resolution WRF is capable of simulating the tremendous rainfall (the maximum rainfall exceeds 2800 mm over a 72-h integration) observed in this case as well as the elongated rainfall pattern in the southwest-northeast direction and heavily concentrated north-south line over southern Taiwan that

was also observed. The good agreement in these features between the model and observations is mainly due to the simulated storm track and intensity being in relatively good agreement with the observed. The typhoon-induced large-scale circulation and Taiwan's unique terrain are the main factors that determine the location of the heavy precipitation.

2. The simulated typhoon intensities are in good agreement with observations after 24 h of model integration when the heavy rainfall occurred over southern Taiwan. The simulated track is in good agreement with the observed track before the typhoon moved inland. However, the model-simulated tracks are too far south and their error becomes larger over the high terrain area and after the typhoon re-emerges over the Taiwan Strait.

3. The results also indicate that convective rain areas were initiated over the Taiwan Strait mainly by the typhoon-induced large-scale circulation and a southwest moisture flow. These convective areas were then intensified by orographic lifting as they propagated inland.

4. The improved microphysics did not improve the track forecast. It did simulate a stronger storm after 12 h of model integration that was in better agreement with observations but later produced a stronger intensity than the control case and what was observed. The stronger storm contributed to more total rainfall that was in better agreement with observations than the control case especially over higher terrain. Though still significant, the improved microphysics resulted in a much better bias as well as maximum rainfall than the control run over southern Taiwan. The new scheme reduced the amount of graupel and increased the amount of snow and cloud ice as with the cases shown in Lang et al. (2011). The stronger storm simulated with the improved physics is a result of less evaporative cooling from cloud droplets and consequently weaker simulated downdrafts. This result is consistent with previous modeling studies (Wang 2002; Zhu and Zhang 2006). Downdrafts are noted to have a negative impact on rapid intensification and the final intensity of simulated storms (Willoughby et al. 1984; Wang 2002).

5. The warm rain only physics resulted in a track and intensity that were very similar to the control case. This result is quite different from previous studies wherein warm rain always produces stronger hurricanes in their early developing stage (Tao et al. 2011). For this case, the total domain-integrated warm rain (cloud and rain) is about the same as the corresponding ice particles (cloud ice, snow and graupel). More than two thirds of the cloud species were from ice for the Katrina case (Tao et al. 2011). For this case, the ice processes are perhaps not the dominant precipitation processes.

6. Both the MYJ and YSU PBL schemes simulated similar patterns in terms of MSLP, track forecast, and surface

rainfall distribution. The YSU PBL scheme simulates 50 W m^{-2} more surface latent heat fluxes over ocean and more total rainfall as well as a higher average rainfall intensity over southern Taiwan than the MYJ scheme. The YSU simulated rainfall intensity is in slightly better agreement with observations. These results are quite different from previous numerical simulations for hurricanes that developed in the Atlantic (i.e., Li and Pu 2008; Nolan et al. 2009a, b). The MYJ scheme usually produces a stronger storm in better agreement with observations for hurricanes that develop in the Atlantic. The YSU PBL scheme has been widely evaluated and adjusted for the East Asian summer monsoon system. Results using different PBL schemes have less sensitivity than those due to the ice microphysics for this typhoon case.

The sensitivity of the Goddard one-moment microphysical and PBL schemes in WRF were tested for one case and compared with observations that only focused on the organization (including track and intensity) and rainfall intensity and statistics. Additional case studies addressing microphysical and PBL processes, including more comprehensive microphysical sensitivity testing (e.g., turning off certain conversion processes from one cloud species to another), will be considered in future research. Recently, a spectral bin microphysics scheme (Khain et al. 2004) and a two-moment scheme (Cheng et al. 2007) were implemented into WRF; additional sensitivity tests with these sophistical microphysical schemes will be needed.

Sensitivity tests on model resolution (horizontal grid spacing from 1 up to 5 km*, and 31 to 81 vertical layers), terrain height (lifting and blocking, see discussion in section 4) and sea surface temperature (surface latent heat fluxes, see discussion in section 5.2) will be conducted and discussed in Part II.

REFERENCES

Anthes, R. A. and S. W. Chang, 1978: Response of the hurricane boundary layer to changes of sea surface temperature in a numerical model. *J. Atmos. Sci.*, **35**, 1240-1255, doi: 10.1175/1520-0469(1978)035<1240:ROTHBL>2.0.CO;2. [Link]

Braun, S. A. and W. K. Tao, 2000: Sensitivity of high-resolution simulations of Hurricane Bob (1991) to planetary boundary layer parameterizations. *Mon. Weather Rev.*, **128**, 3941-3961, doi: 10.1175/1520-0493(2000)129<3941:SOHRSO>2.0.CO;2. [Link]

Chen, C. S., Y. L. Chen, C. L. Liu, P. L. Lin, and W. C. Chen, 2007: Statistics of Heavy Rainfall Occurrences in Taiwan. *Weather Forecast.*, **22**, 981-1002, doi: 10.1175/WAF1033.1. [Link]

Chen, F. and J. Dudhia, 2001: Coupling an advanced land surface - Hydrology model with the Penn State - NCAR MM5 modeling system. Part I: Model implementation and sensitivity. *Mon. Weather Rev.*, **129**, 569-585, doi: 10.1175/1520-0493(2001)129<0569:CAALSH>2.0.CO;2. [Link]

Chen, G. and C. H. Sui, 2010: Characteristics and origin of quasi-biweekly oscillation over the western North Pacific during boreal summer. *J. Geophys. Res.*, **115**, D14113, doi: 10.1029/2009JD013389. [Link]

Cheng, C. T., W. C. Wang, and J. P. Chen, 2007: A modelling study of aerosol impacts on cloud microphysics and radiative properties. *Q. J. R. Meteorol. Soc.*, **133**, 283-297, doi: 10.1002/qj.25. [Link]

Chiao, S. and Y. L. Lin, 2003: Numerical modeling of an orographically enhanced precipitation event associated with Tropical Storm Rachel over Taiwan. *Weather Forecast.*, **18**, 325-344, doi: 10.1175/1520-0434(2003)018<0325:NMOAOE>2.0.CO;2. [Link]

Cotton, W. R., G. J. Tripoli, R. M. Rauber, and E. A. Mulvihill, 1986: Numerical simulation of the effects of varying ice crystal nucleation rates and aggregation processes on orographic snowfall. *J. Climate Appl. Meteorol.*, **25**, 1658-1680, doi: 10.1175/1520-0450(1986)025<1658:NSOTEO>2.0.CO;2. [Link]

Diehl, K. and S. Wurzler, 2004: Heterogeneous drop freezing in the immersion mode: Model calculations considering soluble and insoluble particles in the drops. *J. Atmos. Sci.*, **61**, 2063-2072, doi: 10.1175/1520-0469(2004)061<2063:HDFITI>2.0.CO;2. [Link]

Diehl, K., M. Simmel, and S. Wurzler, 2006: Numerical

Almost all NWP centers are still using 4 or 5 km grid spacing for their real time forecasts.

sensitivity studies on the impact of aerosol properties and drop freezing modes on the glaciation, microphysics, and dynamics of clouds. *J. Geophys. Res.*, **111**, D07202, doi: 10.1029/2005JD005884. [Link]

Fang, X., Y. H. Kuo, and A. Wang, 2011: The impact of Taiwan topography on the predictability of Typhoon Morakot's record-breaking rainfall: A high-resolution ensemble simulation. *Weather Forecast.*, **26**, 613-633, doi: 10.1175/WAF-D-10-05020.1. [Link]

Ferrier, B. S., 1994: A double-moment multiple-phase four-class bulk ice scheme. Part I: Description. *J. Atmos. Sci.*, **51**, 249-280, doi: 10.1175/1520-0469(1994)051 <0249:ADMMPF>2.0.CO;2. [Link]

Fletcher, N. H., 1962: The Physics of Rain Clouds, Cambridge University Press, 386 pp.

Fritsch, J. M. and R. E. Carbone, 2002: Research and development to improve quantitative precipitation forecasts in the warm season: A synopsis of the March 2002 US-WRP Workshop and statement of priority recommendations. Technical report to USWRP Science Committee, 134 pp.

Grell, G. A. and D. Dévényi, 2002: A generalized approach to parameterizing convection combining ensemble and data assimilation techniques. *Geophys. Res. Lett.*, **29**, 1693, doi: 10.1029/2002GL015311. [Link]

Hong, C. C., M. Y. Lee, H. H. Hsu, and J. L. Kuo, 2010: Role of submonthly disturbance and 40-50 day ISO on the extreme rainfall event associated with typhoon Morakot (2009) in southern Taiwan. *Geophys. Res. Lett.*, **37**, L08805, doi: 10.1029/2010GL042761. [Link]

Hong S. Y. and H. L. Pan, 1996: Nonlocal boundary layer vertical diffusion in a medium-range forecast model. *Mon. Weather Rev.*, **124**, 2322-2339, doi: 10.1175/152 0-0493(1996)124<2322:NBLVDI>2.0.CO;2. [Link]

Hong, S. Y. and J. O. J. Lim, 2006: The WRF Single-Moment 6-Class Microphysics Scheme (WSM6). J. *Korean Meteorol. Soc.*, **42**, 129-151.

Hong, S. Y., J. Dudhia, and S. H. Chen, 2004: A revised approach to ice microphysical processes for the bulk parameterization of clouds and precipitation. *Mon. Weather Rev.*, **132**, 103-120, doi: 10.1175/1520-0493 (2004)132<0103:ARATIM>2.0.CO;2. [Link]

Hong, S. Y., Y. Noh, and J. Dudhia, 2006: A new vertical diffusion package with an explicit treatment of entrainment processes. *Mon. Weather Rev.*, **134**, 2318-2341, doi: 10.1175/MWR3199.1. [Link]

Huang, Y. H., C. C. Wu, and Y. Wang, 2011: The influence of island topography on typhoon track deflection. *Mon. Weather Rev.*, **139**, 1708-1727, doi: 10.1175/20 11MWR3560.1. [Link]

Janjić, Z. I., 1990: The step-mountain coordinate: Physical package. *Mon. Weather Rev.*, **118**, 1429-1443, doi: 10.1175/1520-0493(1990)118<1429:TSMCPP>2.0. CO;2. [Link]

Janjić, Z. I., 1996: The surface layer in the NCEP Eta Model, Eleven[th] Conference on Numerical Weather Prediction, Norfolk, VA, 19-23 August. Amer. Meteorol. Soc., Boston, MA, 354-355.

Janjić, Z. I., 2002: Nonsigular implementation of the Mellor-Yamada level 2.5 scheme in the NCEP global model. NCEP Office Note 437, 61 pp (Available at NCEP/ EMC, 5200 Auth Road, Camp Springs, MD 20746).

Jensen, E. J., O. B. Toon, S. A. Vay, J. Ovarlez, R. May, T. P. Bui, C. H. Twohy, B. W. Gandrud, R. F. Pueschel, and U. Schumann, 2001: Prevalence of ice-supersaturated regions in the upper troposphere: Implications for optically thin ice cloud formation. *J. Geophys. Res.*, **106**, 17253-17266, doi: 10.1029/2000JD900526. [Link]

Jian, G. J. and C. C. Wu, 2008: A numerical study of the track deflection of supertyphoon Haitang (2005) prior to its landfall in Taiwan. *Mon. Weather Rev.*, **136**, 598-615, doi: 10.1175/2007MWR2134.1. [Link]

Jou, B. J. D., Y. C. Yu, L. Feng, Y. M. Chen, C. S. Lee, and M. D. Cheng, 2010: Synoptic environment and rainfall characteristics of Typhoon Morakot. *Atmos. Sci.*, **38**, 21-38. (in Chinese)

Khain, A., A. Pokrovsky, M. Pinsky, A. Seifert, and V. Phillips, 2004: Simulation of effects of atmospheric aerosols on deep turbulent convective clouds using a spectral microphysics mixed-phase cumulus cloud model. Part I: Model description and possible applications. *J. Atmos. Sci.*, **61**, 2963-2982, doi: 10.1175/JAS-3350.1. [Link]

Kim, J. and L. Mahrt, 1992: Simple formulation of turbulent mixing in the stable free atmosphere and nocturnal boundary layer. *Tellus A*, **44**, 381-394, doi: 10.1034/ j.1600-0870.1992.t01-4-00003.x. [Link]

Lang, S., W. K. Tao, J. Simpson, R. Cifelli, S. Rutledge, W. Olson, and J. Halverson, 2007: Improving simulations of convective systems from TRMM LBA: Easterly and westerly regimes. *J. Atmos. Sci.*, **64**, 1141-1164, doi: 10.1175/JAS3879.1. [Link]

Lang, S. E., W. K. Tao, X. Zeng, and Y. Li, 2011: Reducing the biases in simulated radar reflectivities from a bulk microphysics scheme: Tropical convective systems. *J. Atmos. Sci.*, **68**, 2306-2320, doi: 10.1175/JA S-D-10-05000.1. [Link]

Li, X. and Z. Pu, 2008: Sensitivity of numerical simulation of early rapid intensification of hurricane Emily (2005) to cloud microphysical and planetary boundary layer parameterization. *Mon. Weather Rev.*, **136**, 4819-4838, doi: 10.1175/2008MWR2366.1. [Link]

Lin, Y. L., R. D. Farley, and H. D. Orville, 1983: Bulk parameterization of the snow field in a cloud model. *J. Climate Appl. Meteor.*, **22**, 1065-1092, doi: 10.11 75/1520-0450(1983)022<1065:BPOTSF>2.0.CO;2. [Link]

McCumber, M., W. K. Tao, J. Simpson, R. Penc, and S. T. Soong, 1991: Comparison of ice-phase microphysical

parameterization schemes using numerical simulations of tropical convection. *J. Appl. Meteorol.*, **30**, 985-1004, doi: 10.1175/1520-0450-30.7.985. [Link]

Mellor, G. L. and T. Yamada, 1982: Development of a turbulence closure model for geophysical fluid problems. *Rev. Geophys.*, **20**, 851-875, doi: 10.1029/RG020i004p00851. [Link]

Meyers, M. P., P. J. DeMott, and W. R. Cotton, 1992: New primary ice-nucleation parameterizations in an explicit cloud model. *J. Appl. Meteorol.*, **31**, 708-721, doi: 10.1175/1520-0450(1992)031<0708:NPINPI>2.0.CO;2. [Link]

Meyers M. P., R. L. Walko, J. Y. Harrington, and W. R. Cotton, 1997: New RAMS cloud microphysics parameterization. Part II: The two-moment scheme. *Atmos. Res.*, **45**, 3-39, doi: 10.1016/S0169-8095(97)00018-5. [Link]

Monin, A. S. and A. M. Obukhov, 1954: Basic laws of turbulent mixing in the surface layer of the atmosphere. *Contrib. Geophys. Inst. Acad. Sci. USSR*, **24**, 163-187. (in Russian)

Morrison, H., J. A. Curry, and V. I. Khvorostyanov, 2005: A new double-moment microphysics parameterization for application in cloud and climate models. Part I: Description. *J. Atmos. Sci.*, **62**, 1665-1677, doi: 10.1175/JAS3446.1. [Link]

Noh, Y., W. G. Cheon, S. Y. Hong, and S. Raasch, 2003: Improvement of the K-profile model for the planetary boundary layer based on large eddy simulation data. *Bound.-Layer Meteor.*, **107**, 401-427, doi: 10.1023/A:1022146015946. [Link]

Nolan, D. S., J. A. Zhang, and D. P. Stern, 2009a: Evaluation of planetary boundary layer parameterizations in tropical cyclones by comparison of *in situ* observations and high-resolution simulations of Hurricane Isabel (2003). Part I: Initialization, maximum winds, and the outer-core boundary layer. *Mon. Weather Rev.*, **137**, 3651-3674, doi: 10.1175/2009MWR2785.1. [Link]

Nolan, D. S., D. P. Stern, and J. A. Zhang, 2009b: Evaluation of planetary boundary layer parameterizations in tropical cyclones by comparison of *in situ* observations and high-resolution simulations of Hurricane Isabel (2003). Part II: Inner-core boundary layer and eyewall structure. *Mon. Weather Rev.*, **137**, 3675-3698, doi: 10.1175/2009MWR2786.1. [Link]

Pruppacher, H. R. and J. D. Klett, 1980: Microphysics of Clouds and Precipitation, Atmospheric and Oceanographic Sciences Library, Vol. 18, 714 pp.

Reisner, J., R. M. Rasmussen, and R. T. Bruintjes, 1998: Explicit forecasting of supercooled liquid water in winter storms using the MM5 mesoscale model. *Q. J. R. Meteorol. Soc.*, **124**, 1071-1107, doi: 10.1256/smsqj.54803. [Link]

Rutledge, S. A. and P. Hobbs, 1983: The mesoscale and mi-croscale structure and organization of clouds and precipitation in midlatitude cyclones. VIII: A model for the "seeder-feeder" process in warm-frontal rainbands. *J. Atmos. Sci.*, **40**, 1185-1206, doi: 10.1175/1520-0469(1983)040<1185:TMAMSA>2.0.CO;2. [Link]

Rutledge, S. A. and P. V. Hobbs, 1984: The mesoscale and microscale structure and organization of clouds and precipitation in midlatitude cyclones. XII: A diagnostic modeling study of precipitation development in narrow cold-frontal rainbands. *J. Atmos. Sci.*, **41**, 2949-2972, doi: 10.1175/1520-0469(1984)041<2949:TMAMSA>2.0.CO;2. [Link]

Skamarock, W. C., J. B. Klemp, J. Dudhia, D. Gill, D. Barker, M. Duda, X. Y. Huang, W. Wang, and J. G. Powers, 2008: A description of the advanced research WRF Version 3. NCAR Technical Note NCAR/TN-475+STR, Boulder, Colorado.

Smagorinsky, J., 1963: General circulation experiments with the primitive equations. *Mon. Weather Rev.*, **91**, 99-164, doi: 10.1175/1520-0493(1963)091<0099:GCEWTP>2.3.CO;2. [Link]

Shi, J. J., W. K. Tao, T. Matsui, A. Hou, S. Lang, C. Peters-Lidard, G. Jackson, R. Cifelli, S. Rutledge, and W. Petersen, 2009: Microphysical properties of the January 20-22 2007 snow events over Canada: Comparison with in-situ and satellite observations. *J. Appl. Meteorol. Climatol.*, **49**, 2246-2266.

Shin, H. and S. Y. Hong, 2009: Quantitative precipitation forecast experiments of heavy rainfall over Jeju Island on 14-16 September 2007 using WRF model. *APJAS*, **45**, 71-89.

Soong, S. T. and Y. Ogura, 1973: A comparison between axisymmetric and slab-symmetric cumulus cloud models. *J. Atmos. Sci.*, **30**, 879-893, doi: 10.1175/1520-0469(1973)030<0879:ACBAAS>2.0.CO;2. [Link]

Starr, D. O'C. and S. K. Cox, 1985: Cirrus clouds. Part I: A cirrus cloud model. *J. Atmos. Sci.*, **42**, 2663-2681, doi: 10.1175/1520-0469(1985)042<2663:CCPIAC>2.0.CO;2. [Link]

Stith, J. L., J. E. Dye, A. Bansemer, A. J. Heymsfield, C. A. Grainger, W. A. Petersen, and R. Cifelli, 2002: Microphysical observations of tropical clouds. *J. Appl. Meteorol.*, **41**, 97-117, doi: 10.1175/1520-0450(2002)041<0097:MOOTC>2.0.CO;2. [Link]

Swann, H., 1998: Sensitivity to the representation of precipitating ice in CRM simulations of deep convection. *Atmos. Res.*, **47-48**, 415-435.

Tao, W. K. and J. Simpson, 1993: Goddard Cumulus Ensemble model. Part I: Model description. *Terr. Atmos. Ocean. Sci.*, **4**, 35-72.

Tao, W. K., J. Simpson, and M. McCumber, 1989: An ice-water saturation adjustment. *Mon. Weather Rev.*, **117**, 231-235, doi: 10.1175/1520-0493(1989)117<0231:AIWSA>2.0.CO;2. [Link]

Tao, W. K., J. Simpson, D. Baker, S. Braun, M. D. Chou, B. Ferrier, D. Johnson, A. Khain, S. Lang, B. Lynn, C. L. Shie, D. Starr, C. H. Sui, Y. Wang, and P. Wetzel, 2003: Microphysics, radiation and surface processes in the Goddard Cumulus Ensemble (GCE) model. *Meteorol. Atmos. Phys.*, **82**, 97-137, doi: 10.1007/s00703-001-0594-7. [Link]

Tao, W. K., J. J. Shi, T. Matsui, A. Hou, S. Lang, C. Peters-Lidard, G. Skofronick-Jackson, W. Petersen, R. Cifelli, and S. Rutledge, 2009: The 20-22 January 2007 snow events over Canada: Microphysical properties, Proceeding of the International Precipitation Workshop, 340-349.

Tao, W. K., J. J. Shi, S. S. Chen, S. Lang, P. L. Lin, S. Y. Hong, C. Perters-Lidard, and A. Hou, 2011: The impact of microphysics on intensity and track of hurricane. *APJAS*, **47**, 1-16.

Thompson, G., R. M. Rasmussen, and K. Manning, 2004: Explicit forecasts of winter precipitation using an improved bulk microphysics scheme. Part I: Description and sensitivity analysis. *Mon. Weather Rev.*, **132**, 519-542, doi: 10.1175/1520-0493(2004)132<0519:EFOWPU>2.0.CO;2. [Link]

Wang, Y., 2002: An explicit simulation of tropical cyclones with a triply nested movable mesh primitive equations model: TCM3. Part II: Model refinements and sensitivity to cloud microphysics parameterization. *Mon. Weather Rev.*, **130**, 3022-3036, doi: 10.1175/1520-0493(2002)130<3022:AESOTC>2.0.CO;2. [Link]

Willoughby, H. E., H. L. Jin, S. J. Lord, and J. M. Piotrowicz, 1984: Hurricane structure and evolution as simulated by an axisymmetric, nonhydrostatic numerical model. *J. Atmos. Sci.*, **41**, 1169-1186, doi: 10.1175/1520-0469(1984)041<1169:HSAEAS>2.0.CO;2. [Link]

Wu, C. C., 2001: Numerical simulation of Typhoon Gladys (1994) and its interaction with Taiwan terrain using the GFDL hurricane model. *Mon. Weather Rev.*, **129**, 1533-1549, doi: 10.1175/1520-0493(2001)129<1533:NSOTGA>2.0.CO;2. [Link]

Wu, C. C. and Y. H. Kuo, 1999: Typhoons affecting Taiwan: Current understanding and future challenges. *Bull. Amer. Meteorol. Soc.*, **80**, 67-80, doi: 10.1175/1520-0477(1999)080<0067:TATCUA>2.0.CO;2. [Link]

Wu, C. C., T. H. Yen, Y. H. Kuo, and W. Wang, 2002: Rainfall simulation associated with Typhoon Herb (1996) near Taiwan. Part I: The topographic effect. *Weather Forecast.*, **17**, 1001-1015, doi: 10.1175/1520-0434(2003)017<1001:RSAWTH>2.0.CO;2. [Link]

Yang, M. J. and L. Ching, 2005: A modeling study of Typhoon Toraji (2001): Physical parameterization sensitivity and topographic effect. *Terr. Atmos. Ocean. Sci.*, **16**, 177-213.

Yang, M. J., D. L. Zhang, and H. L. Huang, 2008: A modeling study of Typhoon Nari (2001) at landfall. Part I: Topographic effects. *J. Atmos. Sci.*, **65**, 3095-3115, doi: 10.1175/2008JAS2453.1. [Link]

Yhang, Y. B. and S. Y. Hong, 2008: Improved physical processes in a regional climate model and their impact on the simulated summer monsoon circulations over East Asia. *J. Climate*, **21**, 963-979.

Zhu, T. and D. L. Zhang, 2006: Numerical simulation of Hurricane Bonnie (1998). Part II: Sensitivity to varying cloud microphysical processes. *J. Atmos. Sci.*, **63**, 109-126, doi: 10.1175/JAS3599.1. [Link]

APPENDIX A: GODDARD MICROPHYSICS

The Goddard Cumulus Ensemble (GCE) model's (Tao and Simpson 1993) one-moment bulk microphysical schemes were implemented into WRF. These schemes are mainly based on Lin et al. (1983) with additional processes from Rutledge and Hobbs (1984). However, the Goddard microphysics schemes have several modifications. First, there is an option to choose either graupel or hail as the third class of ice (McCumber et al. 1991). Graupel has a relatively low density and a high intercept value (i.e., more numerous small particles). In contrast, hail has a relative high density and a low intercept value (i.e., more numerous large particles). These differences can affect not only the description of the hydrometeor population and formation of the anvil-stratiform region but also the relative importance of the microphysical-dynamical-radiative processes. Second, a new saturation technique (Tao et al. 1989) was added. This saturation technique is basically designed to ensure that super saturation (sub-saturation) cannot exist at a grid point that is clear (or cloudy). The saturation scheme is one of the last microphysical processes to be computed. It is only done prior to evaluating the evaporation of rain and deposition or sublimation of snow/graupel/hail. Third, all microphysical processes that do not involve melting, evaporation or sublimation (i.e., transfer rates from one type of hydrometeor to another) are calculated based on one thermodynamic state. This ensures that all of these processes are treated equally. The opposite approach is to have one particular process calculated first modifying the temperature and water vapor content (i.e., through latent heat release) before the next process is computed. Fourth, the sum of all sink processes associated with one species will not exceed its mass. This ensures that the water budget will be balanced in the microphysical calculations.

In addition to the two different three-class ice (3ICE) schemes (i.e., cloud ice, snow and graupel or cloud ice, snow and hail) already implemented into WRF (i.e., versions 2.0 and 3.1), the Goddard microphysics has two other options. The first is equivalent to a two-class ice (2ICE) scheme having only cloud ice and snow. This option may be needed for coarse resolution simulations (i.e., > 5 km grid size). The 2ICE scheme could be applied for winter and frontal

convection (Shi et al. 2009; Tao et al. 2009). The second is warm rain only (cloud water and rain). Recently, the Goddard 3ICE schemes were modified to reduce over-estimated and unrealistic amounts of cloud water and graupel in the stratiform region (Tao et al. 2003; Lang et al. 2007). Various assumptions associated with the saturation technique were also revisited and examined (Tao et al. 2003).

WRF's bulk microphysics schemes require continued examination and improvement. After the study by Lang et al. (2007), it was apparent that the bulk scheme required further modification, as there was still a noticeable bias in the simulated reflectivity distributions aloft with excessive probabilities at higher reflectivity values and peak values that were too strong. The bulk scheme was therefore systematically examined with each individual ice process re-evaluated in light of the aforementioned biases and the assumption that the overall scheme was producing either too much and/or graupel that was too large and possibly likewise for snow. Some logical improvements were made as well. As a result, the following changes to the scheme were adopted. First, in addition to not allowing dry growth[*] following Lang et al. (2007), graupel amounts were directly reduced by effectively lowering the overall riming efficiency, tightening the thresholds for converting rimed snow to graupel, and allowing graupel to sublimate outside of cloud, which was not allowed in the original formulation. As cloud is assumed to be mono-disperse (i.e., having a constant diameter of 20 microns), the graupel riming efficiency was made a function just of graupel size with smaller sizes less efficient and larger sizes more efficient (e.g., Khain et al. 2004). The riming thresholds for converting snow into graupel are fairly arbitrary but can have a large impact on graupel production (Rutledge and Hobbs 1984; Morrison et al. 2005); however, based on comparisons with satellite and radar data (e.g., Lang et al. 2007), the scheme is almost certainly producing too much graupel. The thresholds were therefore adjusted to reduce the amount of graupel, which resulted in more snow. Graupel amounts were also reduced indirectly by reducing the amount of super-cooled cloud water available for riming. The original scheme lacked sufficient means to realistically convert cloud water to cloud ice in the mixed-phase region and relied on somewhat ad hoc settings in the saturation adjust scheme to compensate. Outside of riming, the original scheme did not have the means to convert appreciable amounts of cloud liquid water into ice by the time air parcel temperatures fell to between -12 and -18°C where very little liquid water is typically observed (e.g., Stith et al. 2002). To remedy this, three new processes were added: rime splintering, immersion freezing and contact nucleation.

In addition, the original Fletcher (1962) curve for the number of activated ice nuclei was replaced with the Meyers et al. (1992) formulation throughout the code. In conjunction with these changes, the sequential saturation scheme was relaxed. Water saturation, which is calculated first, was allowed to occur down to much colder temperatures followed by ice saturation, which was allowed to be super saturated as is commonly observed (Jensen et al. 2001; Stith et al. 2002). Preliminary testing showed that these changes alone were not enough to effectively reduce excessive simulated reflectivities at upper levels, so in addition to reducing the amount of graupel, a size-mapping scheme was introduced whereby the characteristic size (i.e., inverse of the slope parameter) of the inverse exponential graupel distribution was specified based on temperature and graupel mixing ratio, effectively lowering the size of graupel particles at colder temperatures while still allowing particles to be large near the melting level and at higher mixing ratios[**]. In addition to these changes to graupel, similar changes were required for snow to bring the core reflectivity probabilities more in line with observations. Snow amounts were reduced by effectively lowering the overall collection efficiency of cloud ice by snow (by again making the efficiency dependent on collector particle size with smaller sizes having a very low efficiency and larger sizes a moderate efficiency), allowing snow to sublimate outside of cloud (not allowed in the original formulation) and accounting for the ambient relative humidity and size of the cloud ice particles in the "Bergeron" process (i.e., Psfi) where cloud ice crystals grow into snow. In the original formulation for Psfi, the ambient relative humidity is implicitly assumed to be 100% with respect to water, which is often incorrect. As with graupel, the characteristic sizes for snow were also mapped according to temperature and mixing ratio with small sizes at colder temperatures and low mixing ratios and larger sizes near the melting level and at higher mixing ratios. In addition to these changes, cloud ice fall speeds were added and accounted for in the sweep volume of those processes involving the accretion of cloud ice. Finally, the threshold for cloud ice auto-conversion to snow was changed to physical units. Table A1 gives a summary of all of the changes along with more details.

APPENDIX B: PLANETARY BOUNDARY LAYER (PBL) SCHEMES

The PBL scheme is basically responsible for vertical sub-grid-scale fluxes due to eddy transports in the whole atmospheric column, not just the boundary layer. Thus, when a PBL scheme is activated, explicit vertical diffusion

---

[*] *Dry growth may not be absolutely zero but should be quite small. Efficiencies are commonly set to very small values.*
[**] *Previous studies have varied the snow/graupel intercept as a function of either mixing ratio (Reisner et al. 1998; Swann 1998; Thompson et al. 2004) or temperature (Hong et al. 2004; Thompson et al. 2004).*

is de-activated with the assumption that the PBL scheme will handle this process. The PBL schemes determine the flux profiles within the well-mixed boundary layer and the stable layer, and thus provide atmospheric tendencies of temperature, moisture (including clouds), and horizontal momentum in the entire atmospheric column. Most PBL schemes consider dry mixing but can also include saturation effects in the vertical stability that determines the mixing. The schemes are one-dimensional and assume that there is a clear scale separation between sub-grid eddies and resolved eddies. This assumption will become less clear at grid sizes below a few hundred meters, where boundary layer eddies may start to be resolved, and in these situations the scheme should be replaced by a fully three-dimensional local sub-grid turbulence scheme such as a turbulence kinetic energy (TKE) diffusion scheme. It is important to understand how assumptions regarding the character of surface fluxes and vertical mixing within the boundary layer affect simulations

Table A1. Microphysical processes modified or added to the original GCE Rutledge and Hobbs based bulk microphysics scheme. "f ( )" indicates "function of". Esi, Egc, and Esc are the collection efficiencies of cloud ice by snow, cloud by graupel and cloud by snow, respectively. Qc0 is the cloud water mixing ratio and ssi, the supersaturation percentage with respect to ice, RH the relative humidity, Vs/g the snow/graupel fall velocity, Bh, i the immersion mode ice nucleating efficiency, and Tair the air temperature. The process nomenclature essentially follows Lin et al. (1983) and Rutledge and Hobbs (1983, 1984). Dgacs and Dgaci are the graupel collection of snow and cloud ice for the dry mode, respectively, and Dgacw the graupel collection of cloud at temperatures below freezing.

Process	Original	Modified	Reference(s)/Notes
Psaut	Efficiency: f (Tair)	Efficiency fixed, threshold: changed from g/g to g/m^{-3}	
Psaci	Esi = 0.1	Esi is f(snow diameter)	See mapping, Fig. 1 in Lang et al. (2011) for size distribution
Praci		Accounts for the addition of cloud ice fall speed	Cloud ice fall speed follows Hong et al. (2004)
Psfi	Independent of RH	Depends on RH, accounts for cloud ice size via Meyers, which depends on ssi	Meyers et al. (1992)
Dgacs/Dgaci		Turned off	See Lang et al. (2007)
Dgacw	Egc = 1.0	Egc is f (graupel diameter)	See mapping, Fig. 1 in Lang et al. (2011) for size distribution
Psacw/Pwacs	Esc = 1.0, Qc0 = 0.5 g kg^{-1}	Esc = 0.45, Qc0 = 1.0 g kg^{-1}	
Rime splintering	None	Added and applied to Psacw/Pgacw, no f (Vs/g) or f (cloud size)	Hallet and Mossop (1974); f (Tair) and splinter mass follow Ferrier (1994)
Pidw/Pidep	Based on Fletcher	Based on Meyers, which depends on ssi	Fletcher (1962); Meyers et al. (1992)
Pint	Based on Fletcher	Based on Meyers, which depends on ssi, previous ice concentration checked	Fletcher (1962); Meyers et al. (1992)
Immersion Freezing	None	Added based on Diehl	Diehl and Wurzler (2004); Diehl et al. (2006), assumes Bh,i = 1.01 e-2 for pollen
Contact Nucleation	None	Added based on Cotton and Pruppacher for Brownian diffusion only	Pruppacher and Klett (1980); Cotton et al. (1986), 500 active nuclei per cc with radii of 0.1 microns
Saturation Adjustment	Sequential based Tao	Modified sequential, iterative, allows for ssi of up to 10%	Tao et al. (2003a)
Snow/Graupel Sublimation	None	Allowed if outside cloud and air subsaturated	
Snow/Graupel size	Based on fixed intercepts	Based on intercepts mapped according to snow/graupel mass and temperature	
Cloud ice fall Speed	None or based on Starr and Cox	Based on Hong	Starr and Cox (1985); Hong et al. (2004)

of convective systems (and typhoons). Two different PBL schemes, the Yonsei University (YSU) PBL and Mellor-Yamada-Janjić (MYJ) PBL scheme, are tested; their main features are described as follows.

(a) Yonsei University (YSU) PBL

The YSU PBL scheme (Hong et al. 2006) is the new version of the Medium-Range Forecast (MRF) PBL scheme (Hong and Pan 1996). This PBL scheme employs a so-called counter-gradient flux for heat and moisture in unstable conditions. It uses enhanced vertical flux coefficients in the PBL, and the PBL height is determined from a critical bulk Richardson number. It handles vertical diffusion with an implicit local scheme, and it is based on the local Ri in the free atmosphere. The main strength of the YSU scheme is the inclusion of an explicit treatment for entrainment processes at the top of the PBL and the use of the counter-gradient terms to represent fluxes due to non-local gradients. The entrainment is made proportional to the surface buoyancy flux in line with results from studies with large-eddy models. The YSU scheme improves the MRF scheme by including an explicit treatment for the entrainment process at the top of the PBL, which can help avoid excessive mixing in the mixed layer during strong wind events. The PBL top is defined using a critical bulk Richardson number of zero (compared to 0.5 in the MRF PBL), so in effect it only depends on the buoyancy profile which, in general, lowers the calculated PBL top compared to MRF.

In the YSU scheme, the PBL height is defined as the level where minimum flux exists inside the inversion layer; according to Hong et al. (2006), in the mixed layer-region ($z \leq h$) the turbulence diffusion equation for a generic prognostic variable C is:

$$\frac{\partial C}{\partial t} = \frac{\partial}{\partial z}\left[K_c\left(\frac{\partial C}{\partial z} - \gamma_c\right) - \overline{(w'c')}_h\left(\frac{z}{h}\right)^3\right] \tag{B1}$$

where K_c is the turbulent diffusion coefficient, γ_c is a correction factor to the local gradient which incorporates the contribution of the large-scale eddies to the total flux, and the second term on the right-hand side represents the asymptotic entrainment flux in the inversion layer. The term $\overline{(w'c')}_h$ is the flux at the inversion layer, w' is the vertical velocity perturbation and c' is the perturbation term for C. The formula keeps the basic concept of Hong et al. (1996) but includes an asymptotic entrainment flux term at the inversion layer $-\overline{(w'c')}_h\left(\frac{z}{h}\right)^3$, which is not included (1996).

Thus, the major difference from Hong et al. (2006) is the *explicit treatment* of the entrainment processes through the second term on the right hand side of Eq. (B1), whereas the entrainment is *implicitly parameterized* by raising h above the minimum flux level in Hong et al. (2006). Above the mixed layer ($z > h$), a local diffusion approach is applied to account for free atmospheric diffusion. In the free atmosphere, the turbulent mixing length and stability formula based on observations (Kim and Mahrt 1992) are utilized. The penetration of entrainment flux above h in Noh et al. (2003) is also considered. Please refer to Hong et al. (2006) for a more comprehensive description of the YSU scheme.

(b) Mellor-Yamada-Janjić (MYJ) PBL

This parameterization of turbulence in the PBL and in the free atmosphere (Janjić 1990, 1996, 2002) represents a nonsingular implementation of the Mellor-Yamada Level 2.5 turbulence closure model (Mellor and Yamada 1982) through the full range of atmospheric turbulent regimes. In this implementation, an upper limit is imposed on the master length scale. This upper limit depends on the TKE as well as the buoyancy and shear of the driving flow. In the unstable range, the functional form of the upper limit is derived from the requirement that the TKE production be nonsingular in the case of growing turbulence. In the stable range, the upper limit is derived from the requirement that the ratio of the variance of the vertical velocity deviation and the TKE cannot be smaller than that corresponding to the regime of vanishing turbulence. The TKE production/dissipation differential equation is solved iteratively. The empirical constants have been revised as well (Janjić 1996, 2002).

The YSU and MYJ PBL schemes differ in the way they calculate surface fluxes and vertical mixing in the PBL. The YSU PBL scheme is a "non-local K" scheme. This approach uses the counter-gradient fluxes to determine the depth of the PBL, and then constrains the vertical diffusion coefficient to a fixed profile within the PBL. The MYJ scheme, however, is a "local K" scheme. The diffusivity coefficients are parameterized as functions of the local Richardson number. The height of the MYJ PBL is estimated from the TKE production. The non-singularity constraint for the TKE production is used under unstable atmosphere conditions.

Both schemes need to be used in combination with a Smagorinsky first-order closure approach (Smagorinsky 1963) that independently handles the horizontal turbulent mixing as a function of the horizontal deformation tensor.